Title

Hinge-migrated fold-scarp model based on an analysis of bed geometry: A study from the Mingyaole anticline, southern foreland of Chinese Tian Shan

Journal

Journal of Geophysical Research: Solid Earth, 120(9)

ISSN

2169-9313

Authors

Li, Tao
Chen, Jie
Thompson, Jessica A
et al.

Publication Date

2015-09-01

DOI

10.1002/2015jb012102

Peer reviewed

AGU PUBLICATIONS

JGR

Journal of Geophysical Research: Solid Earth

RESEARCH ARTICLE
10.1002/2015JB012102

Key Points:
- Folding through curved hinges creates a distinctive fold-scarp geometry
- Scarp slope relies on ratio of hinge migration/width, but scarp height is not
- Shortening rate of the Mingyaole fold is estimated to be ~5.0 mm/a since ~15 ka

Supporting Information:
- Text S1 and Figure S1
- Tables S1 and S2

Correspondence to:
T. Li,
litao.410@163.com

Citation:
Li, T., J. Chen, J. A. Thompson, D. W. Burbank, and H. Yang (2015), Hinge-migrated fold-scarp model based on an analysis of bed geometry: A study from the Mingyaole anticline, southern foreland of Chinese Tian Shan, *J. Geophys. Res. Solid Earth*, *120*, 6592–6613, doi:10.1002/2015JB012102.

Received 8 APR 2015
Accepted 19 AUG 2015
Accepted article online 24 AUG 2015
Published online 21 SEP 2015

Hinge-migrated fold-scarp model based on an analysis of bed geometry: A study from the Mingyaole anticline, southern foreland of Chinese Tian Shan

Tao Li[1], Jie Chen[1], Jessica A. Thompson[2], Douglas W. Burbank[2], and Huili Yang[1]

[1]State Key Laboratory of Earthquake Dynamics, Institute of Geology, China Earthquake Administration, Beijing, China, [2]Department of Earth Science, University of California, Santa Barbara, California, USA

Abstract Fold scarps, a type of geomorphic scarp formed by folding mechanisms of hinge migration or limb rotation, serve to delineate both fault-bend characteristics and folding histories, which can, in turn, illuminate tectonic processes and seismic hazards associated with thrust systems. Because the subsurface geometry of folds is commonly difficult to determine, existing fold-scarp models, which rely on both the fold type and its causative fault geometries, remain uncertain with respect to the kinematic evolution of a given fold. In this paper, we develop a model to illustrate that, irrespective of specific fold type and subsurface geometries, fold-scarp growth in the mechanism of hinge migration can be successfully reconstructed based on analyses of bed geometry. This model reveals that the underlying bed dips and the ratio of hinge migration distance/hinge width control the fold-scarp shape and slope. During initial growth (ratio < 1), the scarp slope increases gradually with migration of the hinge. When the hinge totally exits from its original position (ratio > 1), the slope reaches a maximum, which solely depends on underlying bed dips. The scarp height, however, is independent of the hinge width and can be used to quantify folding magnitude. Application of our model to fold scarps in the Mingyaole anticline in the southern foreland of Chinese Tian Shan indicates that the modeled fold-scarp geometry can roughly match with field observations. The Mingyaole shortening rate is estimated to be $\geq$5.0 mm/a since ~15 ka, such that this single fold has accommodated about half of the regional convergence during the Holocene.

1. Introduction

The fold scarp is a type of geomorphic scarp formed by folding without fault offset of the land surface by underlying causative faults and can be used both to delineate folding kinematics and rates and to reconstruct folding histories. Fold scarps can be kinematically linked with fault-bend folds (Figure 1a) [*Suppe*, 1983; *Suppe et al.*, 1992, 1997; *Ishiyama et al.*, 2004, 2007; *Y. Chen et al.*, 2007; *Hubert-Ferrari et al.*, 2007; *Yue et al.*, 2011; *Le Béon et al.*, 2014], fault-propagation folds (Figure 1b) [*Suppe and Medwedeff*, 1990; *Suppe et al.*, 1992; *Chen et al.*, 2005a], detachment folds (Figure 1c) [*Poblet and McClay*, 1996; *Poblet et al.*, 1997; *Scharer et al.*, 2006; *Goode and Burbank*, 2011], or trishear folds [*Erslev*, 1991; *Allmendinger*, 1998; *Y. Chen et al.*, 2007] that grow in mechanisms of hinge migration or limb rotation [e.g., *Suppe*, 1983; *Poblet and McClay*, 1996; *Shaw et al.*, 2005; *Poblet*, 2012]. Among them, the basic deformation characteristics, geometry, and kinematics of classical fault-bend fold scarps have been thoroughly investigated (Figure 1a) [*Y. Chen et al.*, 2007; *Hubert-Ferrari et al.*, 2007; *Yue et al.*, 2011; *Le Béon et al.*, 2014]. Topographic scarps are formed when the land surface and underlying beds move through an active hinge that is pinned to a fault bend or to a fault tip at depth. Surface traces of the scarp extend along strike of the hinge on the fault hanging wall. The resulting scarp height (H) and slope (ϕ) have a predictable geometric relationship to the fault dips (θ_2 and θ_1) and to incremental slip (S) (Figure 1a):

$$S = H/(\sin\theta_2 - \sin\theta_1), \tag{1}$$

$$\tan(\theta_2 - \phi) = \frac{\sin\theta_1 \cos\left(\frac{\theta_2-\theta_1}{2}\right)}{\cos\left(\frac{\theta_2+\theta_1}{2}\right) - \sin\theta_1 \sin\left(\frac{\theta_2-\theta_1}{2}\right)}. \tag{2}$$

Although classical fault bend and other types of fold-scarp models are well developed, the applicability of these models based on analyzing the fold type and causative fault geometries can be difficult to assess,

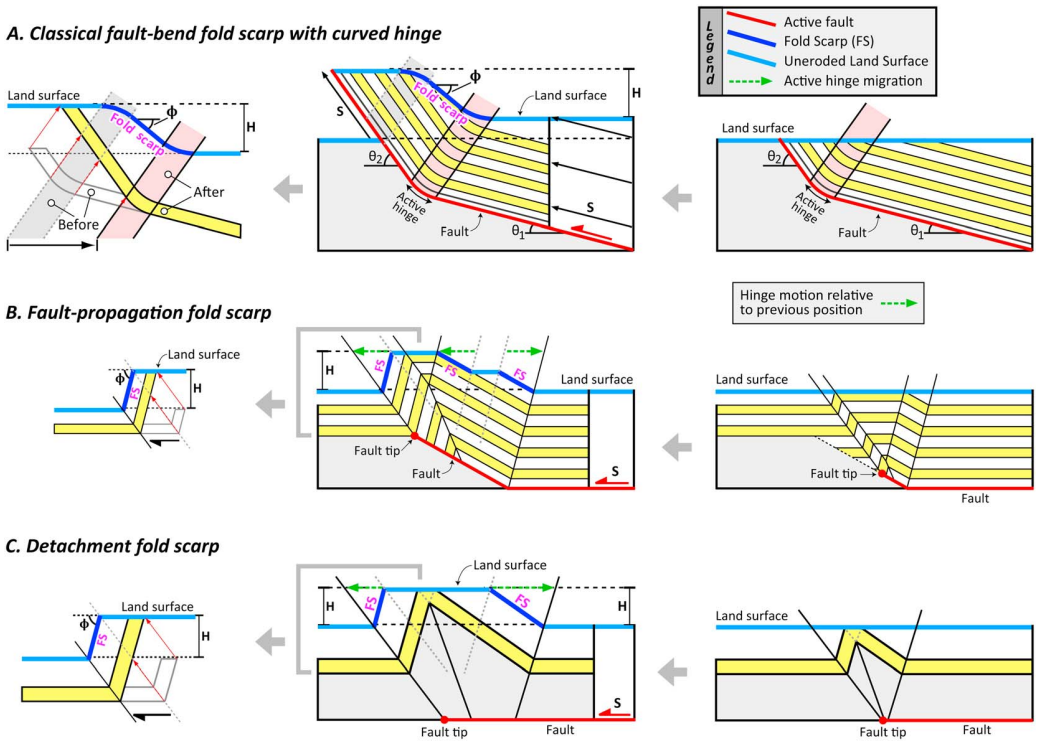

Figure 1. Kinematic models of active fold scarp with hinge migration. *H*: fold-scarp height; ϕ: fold-scarp slope; θ_1 and θ_2: fault dips; *S*: fault slip increment. The green dashed lines with arrows represent the motion of the hinge relative to the beds. (a) Classical fault-bend fold scarp with curved hinge. The fold scarp results from differential uplift across an active hinge pinned to a fault bend at depth. In this model, the land surface and underlying beds on the hanging wall are transported along the curved fault surface. The motion of all materials relative to their portion to the right of the hinge can be described by a set of hinge-parallel slip vectors (thin red lines with arrows in the left figure). Modified from *Yue et al.* [2011] and *Le Béon et al.* [2014]. (b) Fault-propagation fold scarp (FS). The fold scarp results from forward propagation of the fault tip. Modified from *Suppe and Medwedeff* [1990]. (c) Detachment fold scarp (FS) formed due to migration of hinges that are pinned to the detachment surface. Modified from *Poblet and McClay* [1996] and *Poblet et al.* [1997]. The motion of the bed and land surface in Figures 1b and 1c can be described by slip vectors similar to those in Figure 1a.

because the fold subsurface structure is commonly difficult to determine unambiguously. For example, the Mingyaole anticline, located in the southern foreland of Chinese Tian Shan (Figure 2), preserves a series of fold scarps on its two limbs. The fold geometry, however, cannot be well determined due to a lack of high-quality subsurface data, and these fold scarps cannot be reliably analyzed using existing fold-scarp models.

Even though the incremental kinematics of folding is different for varying fold types, the motion of beds that migrates through a hinge can be described by slip vectors parallel to the hinge [*Suppe et al.*, 1997; *Novoa et al.*, 2000], which is similar in all fold types (Figure 1). We argue that, independent of a fold fundamental type and causative fault geometry, fold-scarp growth in the mechanism of hinge migration can be successfully reconstructed based on an analysis of bed geometry controlled by hinge migration. We use this method to develop a kinematic model to illustrate progressive growth of active fold scarps as beds migrate through hinges with varying width. Subsequently, we apply the model to analyze Mingyaole fold scarps and constrain its deformation kinematics and rates. Because the bed geometry can be easily determined from field measurements and/or seismic data, this model, irrespective of specific fold type and subsurface geometries, provides a less limited method to analyze fold-scarp growth.

2. Active Fold-Scarp Model With Hinge Migration

We develop the model comprising a steep (θ_2) bed, a gentle (θ_1) bed, and a bisecting synclinal hinge over which the bed dip changes monotonically (Figure 3). The bed migrates through the hinge without any shear component or secondary deformation (e.g., bending-moment thrusting), therefore conserves

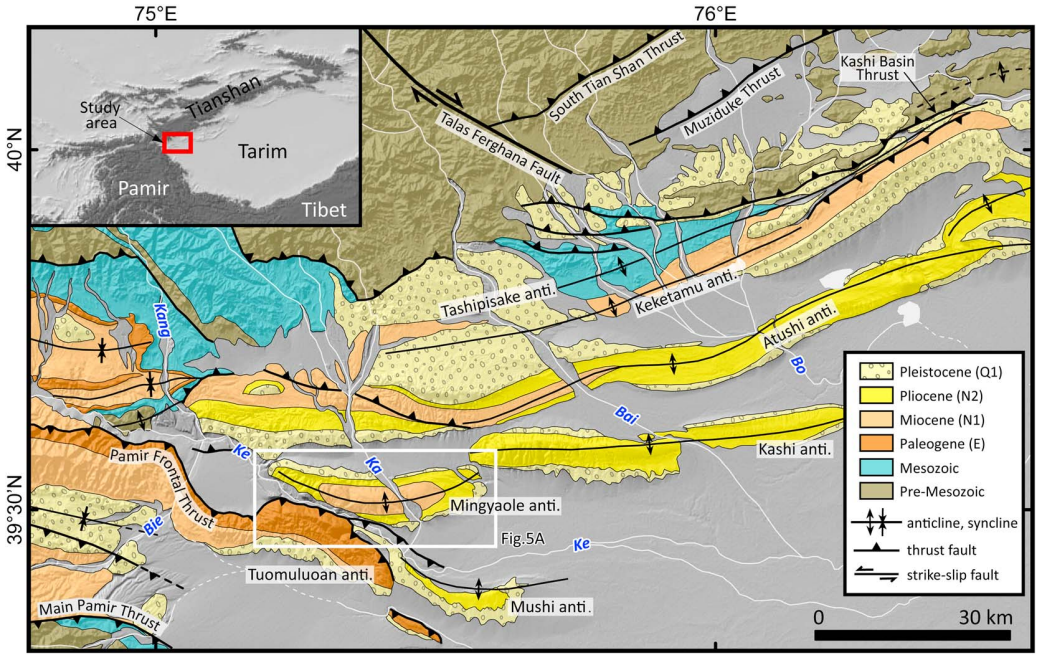

Figure 2. Geologic map of the SW Tian Shan thrust system. Inset shows topographic map of central Asia and the location of the study area. Modified from *Heermance et al.* [2008] and *Thompson et al.* [2015]. Bai: Baishikeremu River, Bie: Biertuokuoyi River, Bo: Boguzi River, Ka: Kalangoulvke River, Kang: Kangsu River, Ke: Kezilesu River.

length, thickness, and continuity. To simplify the model, we assume that the initial terrace surface is flat and the base of the river is fixed, such that the height of terrace surface above the riverbed is equal to the incremental uplift of underlying bed. For ease of visualization, we migrate fold hinges "through" the beds, rather than migrating beds through an apparently fix hinge. This "frame of reference" convenience is irrelevant with respect to the observed or modeled fold-scarp geometry or any derived equations. Fold scarps on terrace surfaces grow progressively with hinge migration. Models with angular, narrow, and wide hinges, respectively, are each illustrated, given that the hinge width can significantly influence the fold-scarp geometry [*Y. Chen et al.*, 2007; *Hubert-Ferrari et al.*, 2007].

2.1. Fold-Scarp Height and Incremental Shortening With Hinge Migration

During migration of the hinge, the bed and overlying terrace surface in θ_1 (gentle) domain will move through the hinge (Figure 3). The motion of the bed and terrace surface relative to their segments to the left of the hinge can be represented by a set of hinge-parallel slip vectors [*Suppe et al.*, 1997; *Novoa et al.*, 2000]. To the left of the hinge, the slip vector of all materials is zero because no relative motion occurs there. Within the span of the hinge, the slip vector increases from zero at the left boundary to the maximum (V) at the right boundary, thereby producing a fold scarp on the terrace surface. All materials to the right of the span uniformly move with the maximum slip vector (V), resulting in parallel terrace surfaces. The slip-vector maximum (V) is geometrically predictable, if the migration distance of the hinge (L) is given (Figures 3 and 4a; see Appendix A1):

$$V = L \cdot (\sin\theta_2 - \sin\theta_1)/\cos\left(\frac{\theta_2 - \theta_1}{2}\right), \tag{3}$$

The slip-vector maximum (V) can be resolved into vertical and horizontal components, which, respectively, raise and laterally move the bed and terrace surface. These two components are equal to the height (H) and incremental shortening (S) of the fold scarp, respectively, and can be calculated by

$$H = L \cdot \cos\left(\frac{\theta_2 + \theta_1}{2}\right)(\sin\theta_2 - \sin\theta_1)/\cos\left(\frac{\theta_2 - \theta_1}{2}\right), \tag{4}$$

$$S = L \cdot \cos\left(\frac{\theta_2 + \theta_1}{2}\right)(\cos\theta_2 - \cos\theta_1)/\cos\left(\frac{\theta_2 - \theta_1}{2}\right). \tag{5}$$

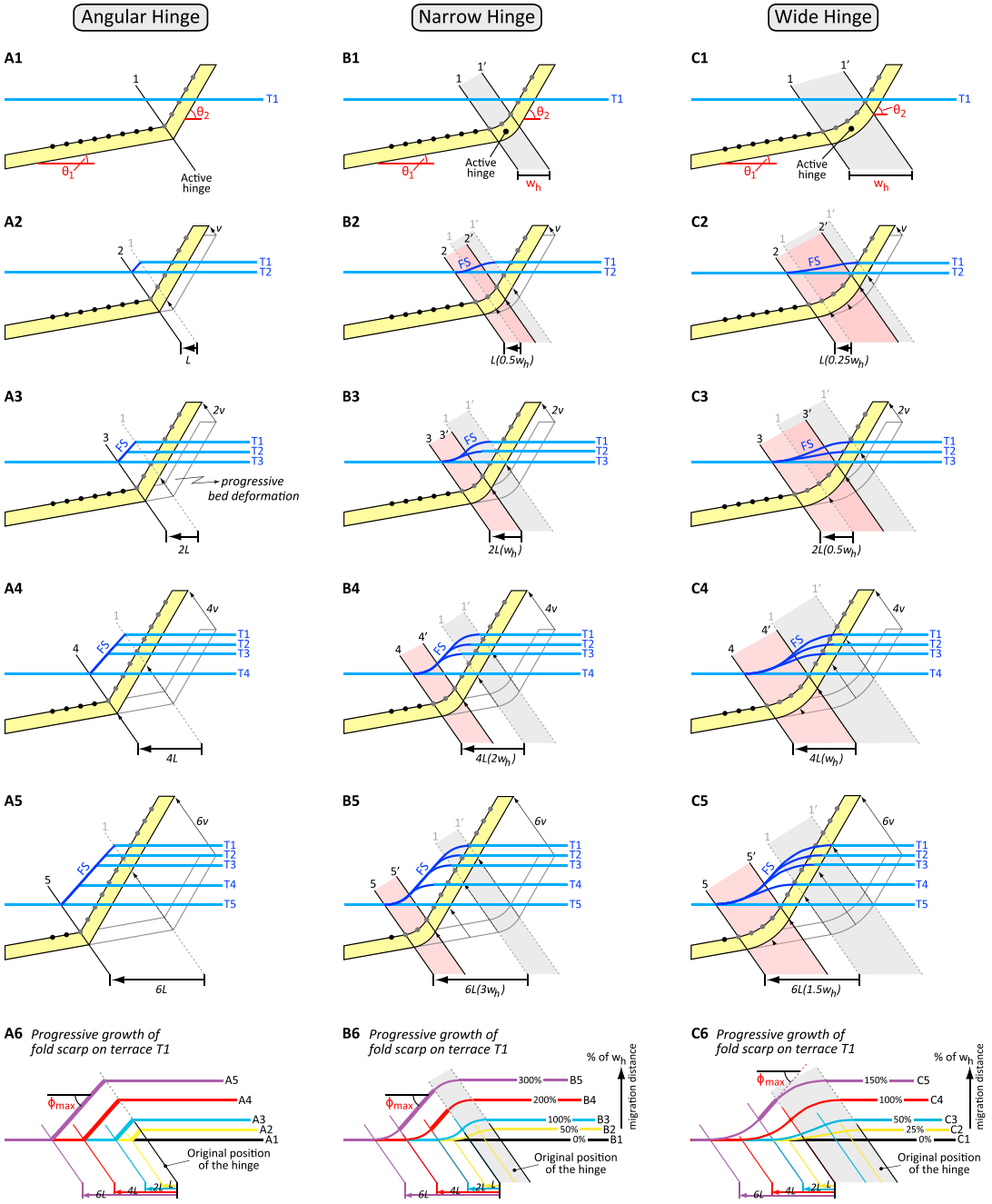

Figure 3. Forward models of active fold scarps with (a1–a6) angular, (b1–b6) narrow, and (c1–c6) wide hinge migration. The gray outlined and yellow beds are, respectively, prior to and after hinge migration that deforms terraces through time. The light blue lines represent river terraces, and the dark blue segments represent fold scarps (FS). Hinge width in Figure 3b is half that in Figure 3c. The fold-scarp shape and slope can be predicted, if the underlying bed dips (θ_1 and θ_2: assumed here to be initially the same for all models), hinge width (w_h), and hinge migration distance (L) are given (see Appendix A). (A1–C1) Terrace T1 formed across an active synclinal hinge. (A2–C2) Active hinge migrates from position 1-1′ (or 1 in Figure A2) to 2-2′ (or 2 in Figure A2). The bed moves through the hinge and is lifted along vectors (thin black lines with arrows) parallel to the hinge. Meanwhile, the terrace T1 is abandoned and also moves along vectors consistent with the bed deformation. Within the passing span of the hinge, a fold scarp is produced on the T1 surface. Note that slope of the fold scarp in A2 is steeper than those in B2 and C2. (A3–A5, B3–B5, and C3–C5) The active hinge migrates gradually to the left, and subsequent terraces are similarly deformed. The fold scarp grows progressively with increasing hinge migration, but its slope reaches a maximum steepness dictated by the dip difference across the hinge. Beyond the passing span of the active hinge, different terraces lie parallel with each other. (A6–C6) Progressive growth of the fold scarp deforms terrace T1 in stages A1–A5, B1–B5, and C1–C5. The fold scarp in Figure A6 achieves its maximum slope immediately when the hinge begins to migrate (Stage A2), whereas the fold scarp in Figures B6 and C6 reaches its maximum slope after stages B3 and C4, respectively, when the active hinge moves sufficiently (100% of the hinge width) away from its original location (bounded by gray dashed lines). Subsequently, fold scarps keep growing in height and width, and the scarp segment of maximum slope extends in length, but its angle remains constant.

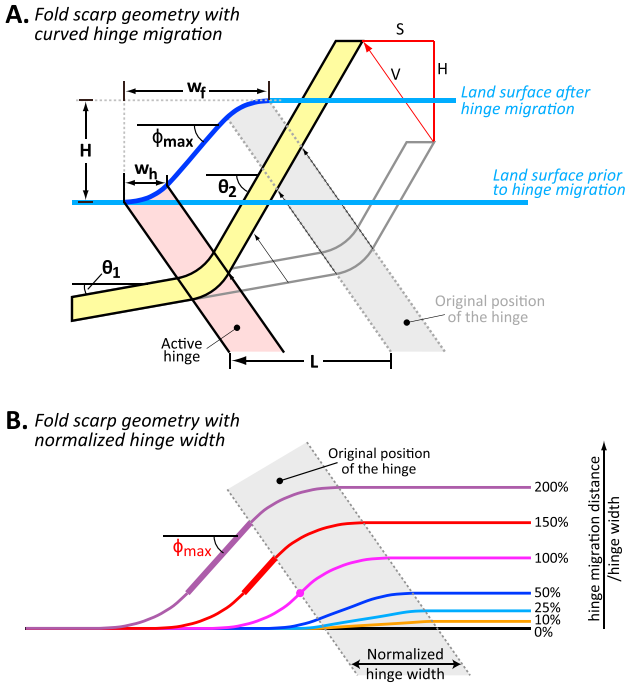

Figure 4. (a) Active fold-scarp geometry with curved-hinge migration. *V*: slip-vector maximum; *H*, *S*, and ϕ_{max}: height, incremental shortening, and maximum slope of the fold scarp, respectively; w_f: fold scarp width; w_h: hinge width; θ_2 and θ_1: steep and gentle bed dips, respectively. See Figure 3 for other legend. (b) Active fold-scarp geometry with normalized hinge width (*N*-w_h). The model is developed for changing shape with increasing ratios of *hinge migration distance/hinge width* and indicates that, when the underlying bed dips are given, the *N*-w_h fold-scarp geometry is only the function of the ratio of *hinge migration distance/hinge width*.

Above formulas can be applied to a fold scarp with an angular, narrow, or wide hinge (Figure 3), thereby indicating that the fold-scarp height and incremental shortening are independent of the hinge width and are only a function of hinge migration distance.

A combination of formulas (4) and (5) defines the geometric relationship between incremental shortening (*S*) and height (*H*) of the fold scarp (Figure 4a):

$$S = H^*(\cos\theta_1 - \cos\theta_2)/(\sin\theta_2 - \sin\theta_1). \quad (6)$$

Note that this incremental shortening is a function of bed migration through the hinge from gentle to steep dip domains (Figures 3 and 4a). Therefore, it represents only the incremental shortening absorbed by the associated migrating hinge but not the total incremental shortening of the fold: a difference from the classical fault-bend fold-scarp model (Figure 1a) [*Y. Chen et al.*, 2007; *Hubert-Ferrari et al.*, 2007; *Yue et al.*, 2011; *Le Béon et al.*, 2014]. Given that active folds commonly include more than one migrating hinge (e.g., Figures 1b and 1c), the total shortening should sum all such incremental shortening. If some active fold scarps are not distinguished or preserved, this method places a minimum limit on the total shortening.

2.2. Fold-Scarp Shape, Slope, and Width With Hinge Migration

In contrast to the height and incremental shortening, the fold-scarp shape, slope, and width can be strongly influenced by the hinge width. For an angular hinge, the fold scarp achieves its maximum slope immediately when the hinge begins to migrate and then remains constant during subsequent fold-scarp growth (Figure 3). For both the narrow and wide hinge, however, the slope increases gradually during initial growth (Figures 3b6 and 3c6). Given an equal migration distance of the hinge, a wider hinge produces a gentler and wider scarp (e.g., Figures 3b2 and 3c2). When the hinge totally exits from its original position, the slope will reach a maximum and will subsequently remain constant even as the migration

distance increases (Figures 3b6 and 3c6). This kinematic process is consistent with classical fault-bend fold-scarp model described by *Y. Chen et al.* [2007] and *Hubert-Ferrari et al.* [2007]. The maximum slope, ϕ_{max}, can be expressed as (see Appendix A2)

$$\tan\left(\phi_{\max}-\frac{\theta_2+\theta_1}{2}\right)=2\tan\left(\frac{\theta_2-\theta_1}{2}\right)-\tan\left(\frac{\theta_2+\theta_1}{2}\right) \tag{7}$$

and is equivalent to the formula (2) of the classical fault-bend fold-scarp model (see Appendix A3). Comparatively, the fold-scarp width (w_f), which can be expressed as

$$w_f = L + w_h, \tag{8}$$

will be influenced by the hinge width (w_h) throughout the entire growth history of the fold scarp.

2.3. Fold-Scarp Geometry With Normalized Hinge Width (N-w_h)

Although the fold-scarp shape, slope, and width are strongly influenced by the hinge width, the fold-scarp geometry with normalized hinge width (N-w_h) is unique, provided that the ratio of hinge migration distance/hinge width (L:w_h) is given (Figure 4b; see Appendix A2). For example, the ratio (L:w_h) of fold scarp in Figure 3b3 is equal to that in Figure 3c4, and both have the same N-w_h geometry, even though their hinge widths are quite different. This geometric characteristic has been previously described by *Hubert-Ferrari et al.* [2007] for classical fault-bend fold scarps: the N-w_h fold-scarp geometry is only the function of the ratio (L:w_h). Whenever bed dips are given, a normalized hinge-width fold-scarp model can be developed for an evolving scarp shape with the ratio of (L:w_h) (Figure 4b).

3. The Mingyaole Anticline

3.1. Tectonic Setting

The E-W trending Tian Shan range, extending ~2500 km across central Asia and bounding northern margin of the Tarim Basin (Figure 2 inset), was created during Cenozoic times as a result of the India-Asia collision [*Molnar and Tapponnier*, 1975; *Yin et al.*, 1998]. Along its SW margin, the Tian Shan is delineated by the South Tian Shan Thrust and Muziduke Thrust (Figure 2), which were reactivated around ~25–20 Ma from fission track dating [*Sobel and Dumitru*, 1997; *Sobel et al.*, 2006]. To the south, up to ~10 km of Cenozoic sediments have accumulated in the foreland basin and have been progressively involved into the Atushi-Kashi fold belt, which is the foreland thrust system of the Tian Shan [*J. Chen et al.*, 2002, 2007; *Scharer et al.*, 2004; *Heermance et al.*, 2008]. The Atushi-Kashi fold belt includes a suite of anticlines and absorbs an average shortening rate of ~5 mm/a since ~1.2 Ma [*Scharer et al.*, 2004]. Fluvial terraces of the Boguzi River across the Atushi fold (Figure 2), the Baishikeremu River across the Kashi fold, and the Kalangoulvke River across the Mingyaole fold are strongly deformed and uplifted [*Chen et al.*, 2005b; *Scharer et al.*, 2006; *Heermance et al.*, 2008; *Li et al.*, 2015], indicating that recent deformation of the fold belt is concentrated on its leading edge.

To the west, the Atushi-Kashi fold belt interferes with the Pamir Frontal Thrust, a fault formed by northward propagation of the Pamir and accommodating a Quaternary shortening rate of ~5–7 mm/a [*Li et al.*, 2012; *Thompson et al.*, 2015]. This interference zone is characterized by widely distributed active thrust faulting and folding [*Li et al.*, 2012, 2013a, 2013b, 2015]. A geodetically defined convergent rate of ~7–10 mm/a [*Yang et al.*, 2008; *Zubovich et al.*, 2010] and strong earthquake activity [*Feng*, 1994] reflect the ongoing and concentrated convergence.

3.2. Mingyaole Stratigraphy, Geomorphology, and Structure

The Mingyaole anticline is located at the leading edge of the Atushi-Kashi fold belt and lies north of the Tuomuluoan and the Mushi anticlines: segments of the Pamir Frontal Thrust (Figure 2). On the surface, the fold exhibits E-W trending topographic relief that is ~35 km long by ~6–10 km wide (Figure 5a). Along its south limb, the SE flowing Kezilesu River, which is the largest longitudinal river in the region, obliquely crosses the fold to produce a deeply incised valley between it and the Tuomuluoan anticline. The south flowing Kalangoulvke River, a tributary of the Kezilesu River, orthogonally crosses the fold to produce a water gap

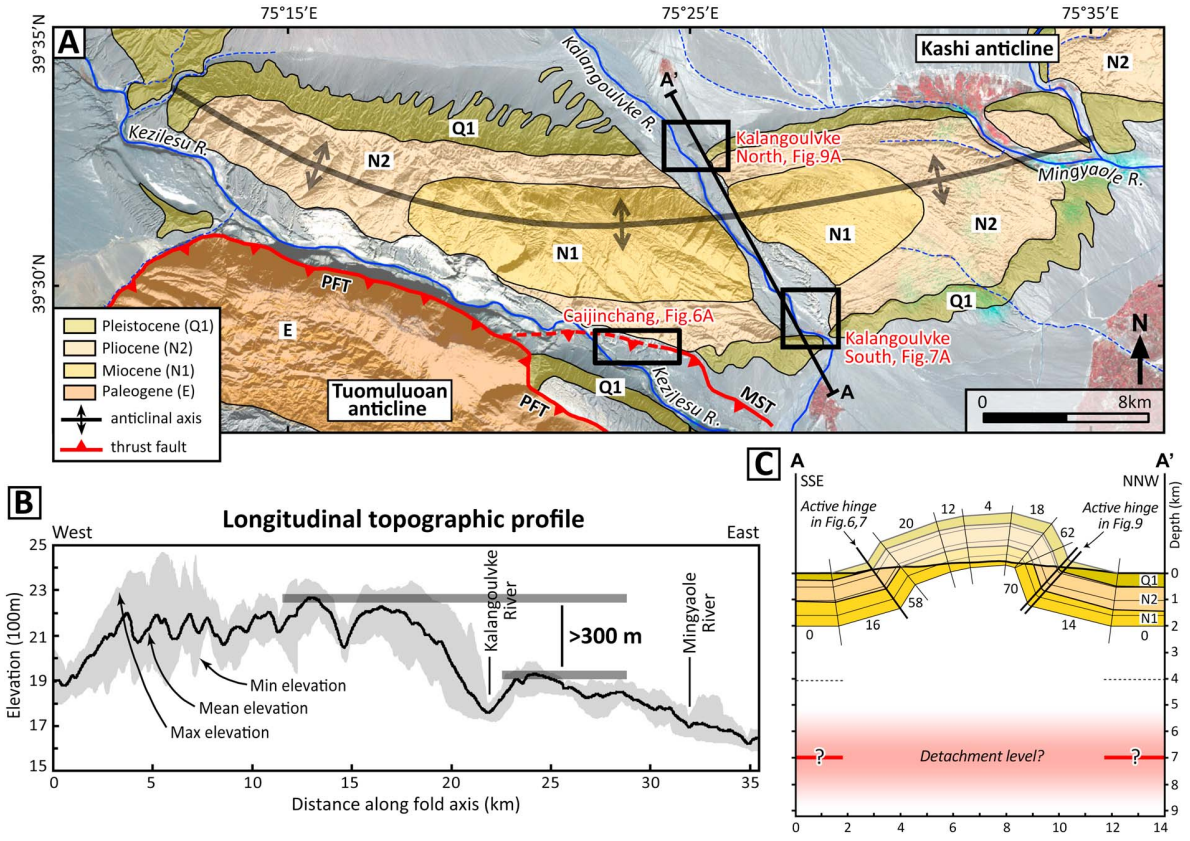

Figure 5. (a) Geologic map of Mingyaole anticline. MST: Mingyaole South Thrust, PFT: Pamir Frontal Thrust. (b) Longitudinal topographic profile of a swath ~5 km wide centered along the crest of the Mingyaole fold. Topography is from the 30 m Advanced Spaceborne Thermal Emission and Reflection Radiometer digital elevation model. Note that the current elevation of fold crest abruptly decreases ~300 m eastward across the Kalangoulvke River. (c) Geologic cross section of Mingyaole fold (for location, see Figure 5a), interpreted from *Scharer et al.* [2004], *Chen et al.* [2005b], and additional field mapping. The detachment surface is speculated to lie ~5–9 km beneath the land surface from seismic data of surrounding area [*Scharer et al.*, 2004; *J. Chen et al.*, 2007; *Heermance et al.*, 2008]. Above the modern topography, the bed shading is lighter.

up to ~3 km wide. The topography of the Mingyaole anticline is strongly modified by these two rivers, and flights of fluvial terraces have been created in the Kezilesu Valley and Kalangoulvke water gap. In addition to these two major rivers, the ephemeral Mingyaole River obliquely crosses the fold eastern tip.

The Mingyaole fold is a box-like anticline with a slightly steeper north limb (~70°) and a gentler south limb (~58°) (Figure 5c). In the fold western part (Figure 5a), the Pamir Frontal Thrust places Paleogene gypsum of the Tuomuluoan anticline over Quaternary (Q1) conglomerates [*Li et al.*, 2012]. To the east, the Mingyaole south limb was ruptured during the 1985 *M*7.4 Wuqia earthquake [*Feng*, 1994], which breached the Mingyaole South Thrust, a northern branch of the Pamir Frontal Thrust.

The lithified sedimentary sequence (Figure 5a) exposed in the fold includes Miocene brownish sandstone and mudstone (N1, Wuqia Group), Pliocene gray-yellow and gray-green sandstone alternating with mudstone (N2, Atushi Formation), and Pleistocene gray dark massive conglomerate of (Q1, Xiyu Formation). The N2-N1 units are conformable, but a time-transgressive contact separates them from the overlying syntectonic Q1 conglomerate [*Chen et al.*, 2005b].

The Mingyaole fold is strongly eroded: although the structural relief of the Q1/N2 contact is up to 2 km (Figure 5c) [*Chen et al.*, 2005b], the present topographic relief is only 500–800 m. The topographic peak coincides with outcrops of the erosion-resistant Q1 conglomerate on each limb, implying a fundamental control of bedrock erodibility on the fold topography. One significant topographic feature is illustrated by the longitudinal profile of the fold crest: the elevation abruptly drops by ~300 m eastward across the

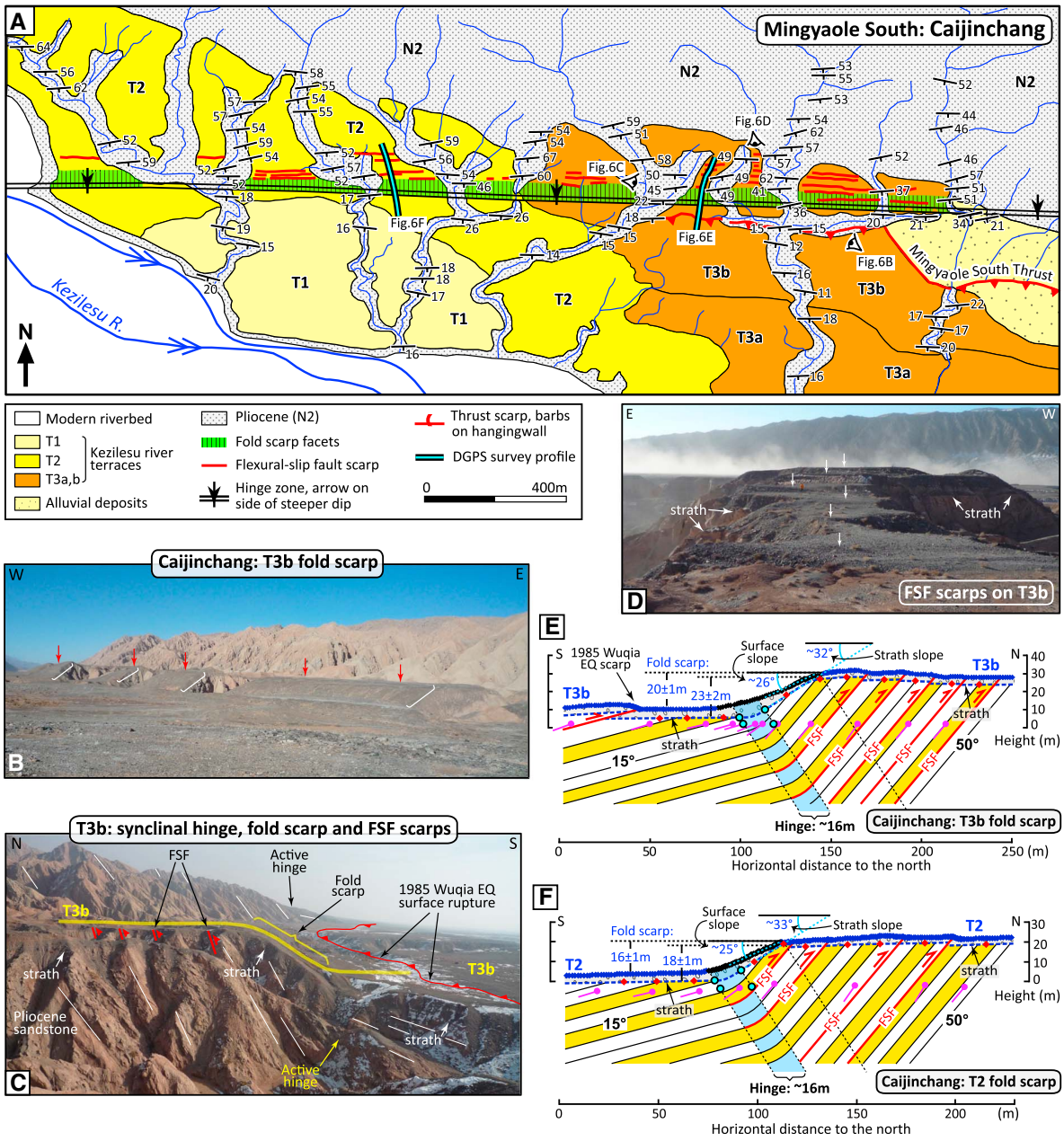

Figure 6. (a) Geologic and geomorphic map of the Kezilesu River terraces at Caijinchang on Mingyaole south limb, as interpreted from Google Earth images and field observations. Alluvial deposits from the northern bedrock hill are younger than the T3b surface. Map area is shown in Figure 5a. (b–d) Photographs of the fold scarp (red arrows and white brackets in Figure 6b), flexural-slip fault (FSF) scarps, and outcrops. See viewpoints in Figure 6a. (e and f) Topographic survey profiles of the fold scarp on T3b and T2 surfaces; see Figure 6a for the locations. The strath surface (discrete red points) is delineated by measurements of the land surface and thickness of capping gravels. The hinge boundaries (light blue circles) are determined from field observations. Bed dips and land-surface slopes are displayed with no vertical exaggeration.

Kalangoulvke River (Figure 5b). We speculate that this abrupt change may derive from lateral erosion by the paleoriver. During initial fold growth, the river apparently had enough stream power (versus the strength of the very young strata that form "bedrock" of the fold) to laterally bevel all the uplifted rocks to its east. At some point, the rock-uplift rate of the fold outpaced the ability of the river to bevel the eastern fold crest, and the fold emerged above the floodplain at an elevation ~300 m below its crest to the west of the river.

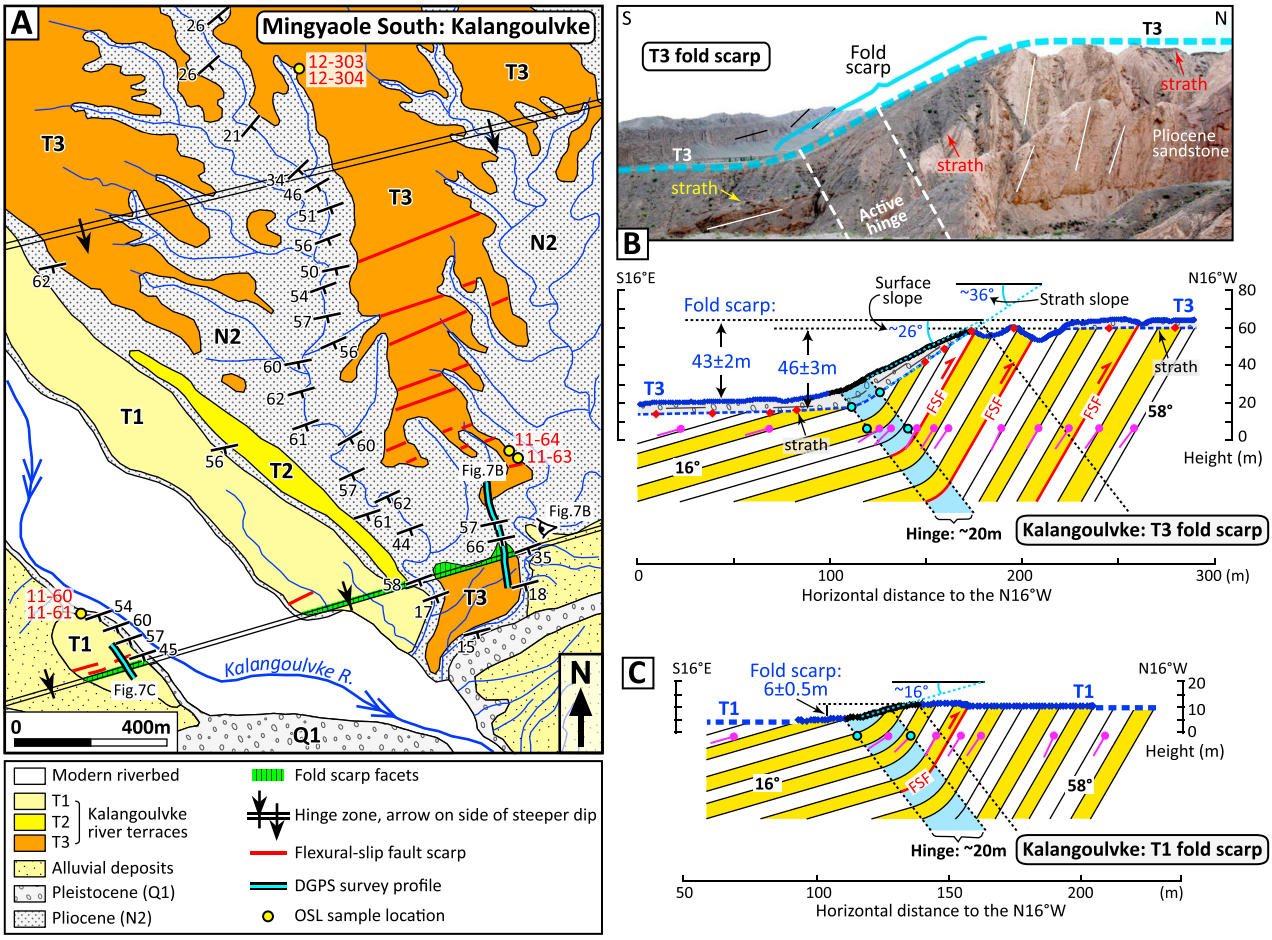

Figure 7. (a) Geologic and geomorphic map of the Kalangoulvke River terraces on Mingyaole south limb. Alluvial deposits were deposited in several stages here and span a wide time interval but should be younger than Q1 conglomerates. Map area is shown in Figure 5a. (b) Photograph (viewpoint in Figure 7a) and topographic survey profile of the fold scarp on the T3 surface. (c) Topographic survey profile of the fold scarp on the T1 surface. FSF: flexural-slip fault. The strath surface (discrete red points) and hinge boundaries (light blue circles) are delineated using a method similar to Caijinchang (see legend for Figures 6e and 6f).

Integration of new geologic mapping data along the Kalangoulvke River valley with data in *Scharer et al.* [2004] and *Chen et al.* [2005b] constrains the cross section of the Mingyaole anticline (Figure 5c). The basal detachment surface is interpreted to lie along the flat-lying Paleogene gypsum beds ~5–9 km beneath the land surface as deduced from seismic data across the Atushi and Kashi anticlines [*Scharer et al.*, 2004; *J. Chen et al.*, 2007; *Heermance et al.*, 2008]. Although *Scharer et al.* [2004] and *Chen et al.* [2005b] interpret this fold as a detachment fold, the subsurface geometry remains uncertain due to a lack of high-quality seismic data. Total shortening, estimated from the excess-area method [*Epard and Groshong*, 1993], is ~1.7–3.0 km. Based on the initiation age of ~1.6 Ma from magnetostratigraphic and burial cosmogenic ages in the Kalangoulvke River valley [*Chen et al.*, 2005b; *Thompson*, 2013], the average shortening rate is ~1.1–1.9 mm/a. The fold remains active, and fluvial terraces are not only tilted [*Chen et al.*, 2005b; *Scharer et al.*, 2006; *Li et al.*, 2013b, 2015] but are deformed by a series of fold scarps at Caijinchang and Kalangoulvke River valley on both limbs.

4. The Mingyaole Fold Scarps

4.1. Field Techniques: Topographic Survey and Structural Measurement

Terrace surfaces in the Mingyaole anticline are clearly deformed in response to fold growth (Figures 6, 7, and 9). To quantify the deformation, we surveyed terrace surfaces using an E-survey 660 Real-Time Kinematics dGPS

system which yielded relative vertical and horizontal precisions of <4 cm: less than the geomorphic noise due to natural ground-surface irregularities. Survey lines were roughly linear and avoided areas where the original terrace surface was mantled by young colluvial or alluvial deposits, as well as areas of artificial modification. Survey points were projected perpendicular to the hinge, which produced a deformation pattern of each terrace surface. At Caijinchang and Kalangoulvke South, the capping fluvial gravels of high terraces were partially eroded near the fold-scarp top and were redeposited near the fold-scarp foot, thereby causing a decrease in the original scarp slope. In such scenarios, we also discretely measured the thickness of capping gravels where exposed along erosional faces, especially near the active hinge, using TruPulse 200 laser pointers (Figures 6e, 6f, and 7b). These data, combined with dGPS survey points of terrace surfaces, delineate the deformation pattern of strata surfaces.

Because terrace deformation is closely related to underlying structures, we measured bed strike/dips in the field and projected them to topographic survey profiles of terraces, such that dips presented were apparent dips (Figures 6, 7, and 9). The hinge width, which can significantly influence the fold-scarp geometry (Figure 3), was carefully surveyed and estimated. On the south limb, the hinge is narrow (~16–20 m; Figures 6 and 7) and the underlying beds are well exposed. We constrain the hinge width based on (i) hinge boundary locations were defined in the field, and then surveyed using dGPS, from which the hinge width can be obtained; (ii) for the strath surface of older (higher) terraces, the width of curved segment surrounding the hinge is interpreted to represent the hinge width. On the north limb, the hinge is wide (Figure 9), and we approximately constrain its boundaries and width by the zone through which the dip of underlying beds changes progressively.

4.2. South Limb Fold Scarps at Caijinchang

Caijinchang is located on the south limb and the approximate midpoint along the length of the Mingyaole fold (Figure 5a). Uplift of the fold, activity of the Mingyaole South Thrust, and strong incision of the Kezilesu River create flights of fluvial terraces (Figure 6a). These terraces are strath terraces, which are beveled into the N2 sandstone and mudstone and Q1 conglomerate and are presently capped by well-rounded fluvial gravels. Based on interpretation of Google Earth images and field observations, we categorized fluvial terraces into three major divisions with respect to their relative heights above the modern riverbed (Figure 6a). Overlying the dip domain of ~15°, the T2 and T1 surfaces are ~30–40 and ~8–15 m high, respectively. The T3 surface is ~10 m higher than the T2 surface and can be subdivided into T3a and T3b surfaces. Based on ^{10}Be cosmogenic nuclide depth profile dating (six coarse sand samples were taken from an ~2.0 m deep hole) of *Thompson* [2013], the T2 surface has an exposure, i.e., abandonment, age of 8.0 ± 1.1 ka.

On the T3b and T2 surfaces, an E-W trending topographic scarp faces south (Figures 6a–6c). The height and slope of the scarp on T3b and T2 surfaces are 20 ± 1 m and ~26° and 16 ± 1 m and ~25°, respectively (Figures 6e and 6f). Because the initial fold-scarp slope on terrace surfaces was subsequently modified by partially erosion and redeposition (especially near the scarp crest and toe), we also measured the T3b and T2 strath surfaces (Figures 6e and 6f), which have scarp slopes of ~32° and ~33°, respectively: ~6–8° higher than the land-surface slopes above them. Geologic mapping beneath the slope of the scarp shows no evidence of faulting. Instead an ~16 m wide synclinal hinge separates beds dipping 48–59° in the north from those dipping 15–20° in the south. Overall, above observations argue that the scarp is a simple fold scarp.

On the upper tread (north side) of the fold scarp, numerous flexural-slip fault scarps disturb the T3b and T2 surfaces (Figures 6a, 6c, and 6d). Terrace surfaces are locally tilted near these fault scarps, whose heights span a wide range from ~0.2 to 4.2 m [*Li et al*., 2015]. Such fault scarps can be attributed to the local compressive stress near the active hinge and to the differential strength of underlying beds [*Yeats et al*., 1981, 1997].

4.3. South Limb Fold Scarps at Kalangoulvke

The synclinal hinge in Caijinchang can be traced eastward ~6–8 km to Kalangoulvke River valley (Figure 5a), where terrace surfaces are also deformed by a fold scarp (Figure 7). At this site, three strath terraces of different ages are present (Figure 7a). The T3 and T1 surfaces are spatially extensive, compared with the more local preservation of the T2 surface. Overlying the bed domain of ~16°, heights of T3, T2, and T1 surfaces are ~20–23 m, ~10 m, and ~4–6 m, respectively. Notably, in contrast to the Caijinchang site, the T3 to T1 surfaces were created by the transverse Kalangoulvke River, rather than the SE flowing Kezilesu River.

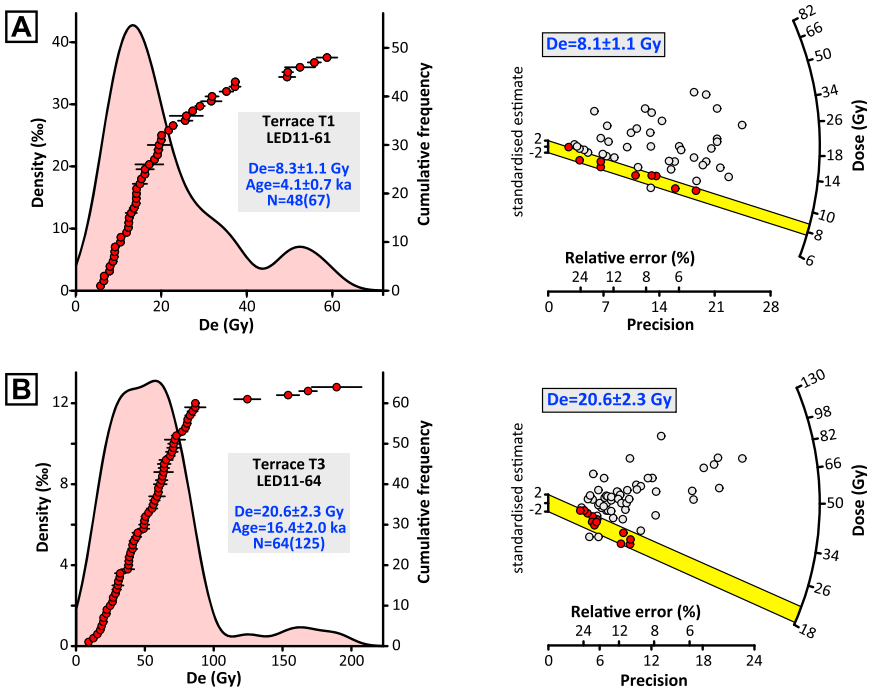

Figure 8. OSL dating results for samples (a) LED11-61 and (b) LED11-64 collected from terraces T1 and T3, respectively, at Kalangoulvke South (see supporting information for other four sample results). (left) The MAM (minimum age model) fit (pink zone with black solid outer line) and cumulative frequency (red circle with 1σ standard error). *N* is the number of accepted aliquots (out of total aliquots measured). (right) Radial plots of the same data. The red circles and yellow bars represent the aliquots and component used in the MAM fit.

The ages of T3 and T1 terraces are well defined by six optically stimulated luminescence (OSL) samples taken from silt-fine sand lenses in fluvial deposits (Figure 8 and Table 1). All samples are analyzed using a single aliquot regeneration (SAR) protocol [*Murray and Wintle*, 2003] on small aliquots of the 125–250 μm grain-size quartz fraction. Technical details regarding sample preparation, measurement, and analysis are given in Table 1 and in the supporting information. Four samples taken from the T3 terrace give ages in a range of ~12–16 ka (Table 1), and we use the average age of 14.6 ± 2.6 ka as the terrace age. This age correlates with the age of regional Last Glacial Maximum terrace of ~14–18 ka [*Li et al.*, 2012, 2013a; *Thompson*, 2013] and implies that the T3 terrace formed in response to climate change. Ages of the two samples taken from the T1 surface are similar, and their average age of 4.5 ± 0.8 ka is used to represent the terrace age.

The synclinal hinge near the fold scarp trends ENE, is ~20 m wide, and separates beds that dip ~58° in the north from beds dipping ~16° in the south (Figures 7a and 7b). This synclinal hinge is clearly associated with the south

Table 1. OSL Dating Results for Samples Collected From Fluvial Terraces at Kalangoulvke South[a]

Sample No.	Latitude/Longitude	Depth (m)	Aliquots[b]	MAM[c] *De* (Gyr)	Dose Rate[d] (Gyr/ka)	MAM[c] Age (ka)	Terrace
LED11-60	39.48554°N/75.46374°E	2.6	52(92)	9.7 ± 1.3	2.0 ± 0.1	4.8 ± 0.9	T1
LED11-61	39.48554°N/75.46374°E	1.0	48(67)	8.3 ± 1.1	2.0 ± 0.1	4.1 ± 0.7	T1
LED11-63	39.48922°N/75.47747°E	1.0	55(77)	24.7 ± 3.1	1.6 ± 0.1	15.5 ± 2.1	T3
LED11-64	39.48945°N/75.47720°E	1.2	64(125)	20.6 ± 2.3	1.3 ± 0.1	16.4 ± 2.0	T3
LED12-303	39.49852°N/75.47072°E	2.3	49(81)	21.4 ± 3.0	1.5 ± 0.2	14.7 ± 3.3	T3
LED12-304	39.49852°N/75.47072°E	1.3	58(102)	26.2 ± 2.8	2.2 ± 0.2	11.8 ± 2.6	T3

[a]All samples were analyzed using a single aliquot regeneration (SAR) protocol [*Murray and Wintle*, 2003] on small aliquot of quartz grains. Measurements were made at the State Key Laboratory of Earthquake Dynamics, Institute of Geology, China Earthquake Administration. Technical details regarding sample preparation, measurement, and analysis are given in the supporting information.
[b]Number of accepted aliquots used in *De* (equivalent dose) calculation, out of total aliquots measured.
[c]MAM (minimum age model) [*Galbraith and Laslett*, 1993] applied to calculate the *De* and age.
[d]Determined from the concentrations of U, Th, and K (Ra included for sample LED12-303; see supporting information), and the water content of sediment, plus a contribution from cosmic rays.

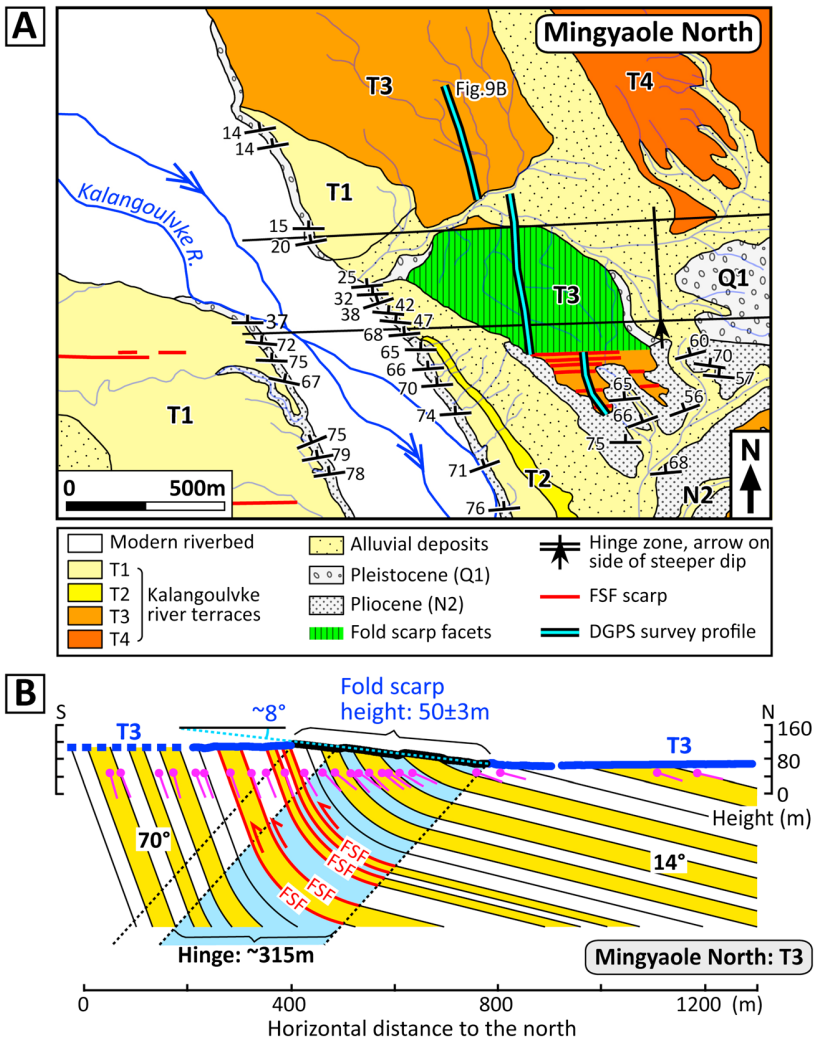

Figure 9. (a) Geologic and geomorphic map of the Kalangoulvke River terraces on Mingyaole north limb. Alluvial deposits were deposited in several stages, similar to those in Figure 7a. Map area is shown in Figure 5a. (b) Topographic survey profile of the fold scarp on the T3 surface. FSF: flexural-slip fault. Note that the wider hinge yields a lower scarp slope than that on the south limb.

facing fold scarp on the T3 and T1 surfaces. Although the T3 fold scarp has been significantly dissected (Figure 7b), its height and slope can be defined as 43 ± 2 m and ~26° on the land surface and $\sim 46 \pm 3$ m and ~36° on the strath surface. The T1 fold scarp is well preserved, displaying a height and slope of 6 ± 0.5 m and ~16° on the land surface (Figure 7c).

Similar to the Caijinchang fold scarp, the upper tread (north side) of the terrace is offset by several flexural-slip fault scarps (Figure 7). Their heights on T3 and T1 surfaces are ~0.2–3.0 m and <1.0 m, respectively. Despite local tilting near these flexural-slip fault scarps, terrace surfaces are generally subparallel with the modern riverbed and imply no obvious tilting of the entire surface.

4.4. North Limb Fold Scarps at Kalangoulvke

On Mingyaole north limb, four Kalangoulvke river terraces are present (Figure 9a). The T4, T3, and T1 surfaces are spatially widespread, with heights of ~55 m, ~19–22 m, and ~4–5 m, respectively, overlying the dip domain of ~14°. Because (i) heights of T3 and T1 surfaces are similar to heights of T3 and T1 surfaces at Kalangoulvke South, respectively, and (ii) both T3 and T1 surfaces on two limbs are spatially extensive, we correlate terraces T3 and T1 at this site with T3 and T1 at Kalangoulvke South, respectively. On the T3 surface,

Table 2. Predicted Slope and Shortening Increment[a] of Mingyaole's Fold Scarp Calculated From Field Observations

Terrace Surface	Fold Scarp		Bed Dip[c] (θ_2/θ_1)	Hinge Width[d] (w_h)	Predicted Slope[a] (ϕ_{max}) (2σ)	Migration Distance[a] (2σ) (% of Hinge Width)	Shortening Increment[a] (2σ)	Shortening Rate[a] (2σ)
	Height (H)	Slope (ϕ)						
Caijinchang T3b	20 ± 1 m	~33°[b]	50 ± 5°/15 ± 2°	16 ± 3 m	32 ± 6°	$44^{+9/-6}$ m (~280%)	$12.7^{+2.0/-1.8}$ m	-
Caijinchang T2	16 ± 1 m	~32°[b]	50 ± 5°/15 ± 2°	16 ± 3 m	32 ± 6°	$35^{+8/-6}$ m (~220%)	$10.1^{+1.9/-1.6}$ m	$1.2^{+0.6/-0.3}$ mm/a
Kalangoulvke South T3	43 ± 2 m	~36°[b]	58 ± 6°/16 ± 2°	20 ± 4 m	38 ± 6°	$87^{+16/-12}$ m (~440%)	$32.2^{+5.4/-4.5}$ m	$2.0^{+1.5/-0.5}$ mm/a
Kalangoulvke South T1	6 ± 0.5 m	~16°	58 ± 6°/16 ± 2°	20 ± 4 m	38 ± 6°	$12^{+3/-2}$ m (~60%)	$4.5^{+1.0/-0.9}$ m	$1.0^{+0.4/-0.2}$ mm/a
Kalangoulvke North T3	50 ± 3 m	~8°	70 ± 7°/14 ± 2°	315 ± 30 m	51 ± 7°	$85^{+14/-12}$ m (~30%)	$44.6^{+9.1/-7.2}$ m	$2.9^{+2.0/-0.7}$ mm/a

[a]Predicted slope and shortening increment are calculated from equations (7) and (6), respectively. The results are presented with the most probable value and minimum and maximum 95% confidence values resulting from Monte Carlo simulations of uncertainties (Appendix B).
[b]Slopes of the fold scarp on strath surfaces.
[c]Errors of bed dips (θ_2 and θ_1) assume ±10%.
[d]Errors of hinge width (w_h) assume ±20%.

a scarp faces north with a height of 50 ± 3 m and a slope of ~8.0° (Figure 9b). This scarp is spatially associated with an ~315 m wide synclinal hinge across which the dip of underlying beds gradually decreases from ~70° in the south to ~14° in the north, thereby exhibiting typical characteristics of a fold scarp. On the upper tread directly south of the fold scarp, flexural-slip fault scarps also disrupt the terrace surface (Figure 9). Away from the fold scarp and flexural-slip fault scarps, the T3 surface is not obviously tilted. The T1 surface has been strongly eroded near the synclinal hinge, making it difficult to quantify the fold-scarp geometry from topographic data.

5. Application of the Model to the Mingyaole Fold Scarps

Field surveys of fold scarps flanking the Mingyaole anticline underpin three basic observations: (i) each fold scarp coincides with and can be traced along its synclinal hinge, (ii) a given fold scarp displays increasing heights with greater terrace age, and (iii) terrace surfaces are not significantly tilted away from the hinge or the fold scarp. These characteristics indicate that the fold scarp was formed by kink-band migration due to material movement through a hinge (Figures 1 and 3) [*Suppe et al.*, 1992, 1997; *Scharer et al.*, 2006; *Hubert-Ferrari et al.*, 2007]. Because the basic type and subsurface geometry of the Mingyaole anticline can only be weakly documented from surface data, the kinematic history of these fold scarps cannot be adequately analyzed using previous models (Figure 1). Instead, our new model, one based on an analysis of exposed bed geometry with hinge migration, can be applied.

5.1. Field Observation Versus Model Prediction of the Mingyaole Fold-Scarp Geometry

The hinge migration distance L is a key parameter in our model (see section 2 above). This distance cannot be determined directly but can be readily calculated from equations (translated from equations (4) and (8), respectively)

$$L = H \cdot \cos\left(\frac{\theta_2 - \theta_1}{2}\right) \Big/ \left[\cos\left(\frac{\theta_2 + \theta_1}{2}\right)(\sin\theta_2 - \sin\theta_1)\right] \quad (9)$$

or

$$L = w_f - w_h, \quad (10)$$

where H (fold-scarp height), θ_2 and θ_1 (bed dips), w_f (fold-scarp width), and w_h (hinge width) can be determined from field survey data. Considering that w_f and w_h have relatively large field uncertainties, we use the fold-scarp height (H) (equation (9)) to calculate the migration distance (L) of the Mingyale fold scarps (Table 2). By combining the calculated L with hinge width (w_h) and bed dips (θ_2 and θ_1), the shape and slope of the Mingyaole fold scarp can be predicted (see Appendix A2). A comparison of modeled results with

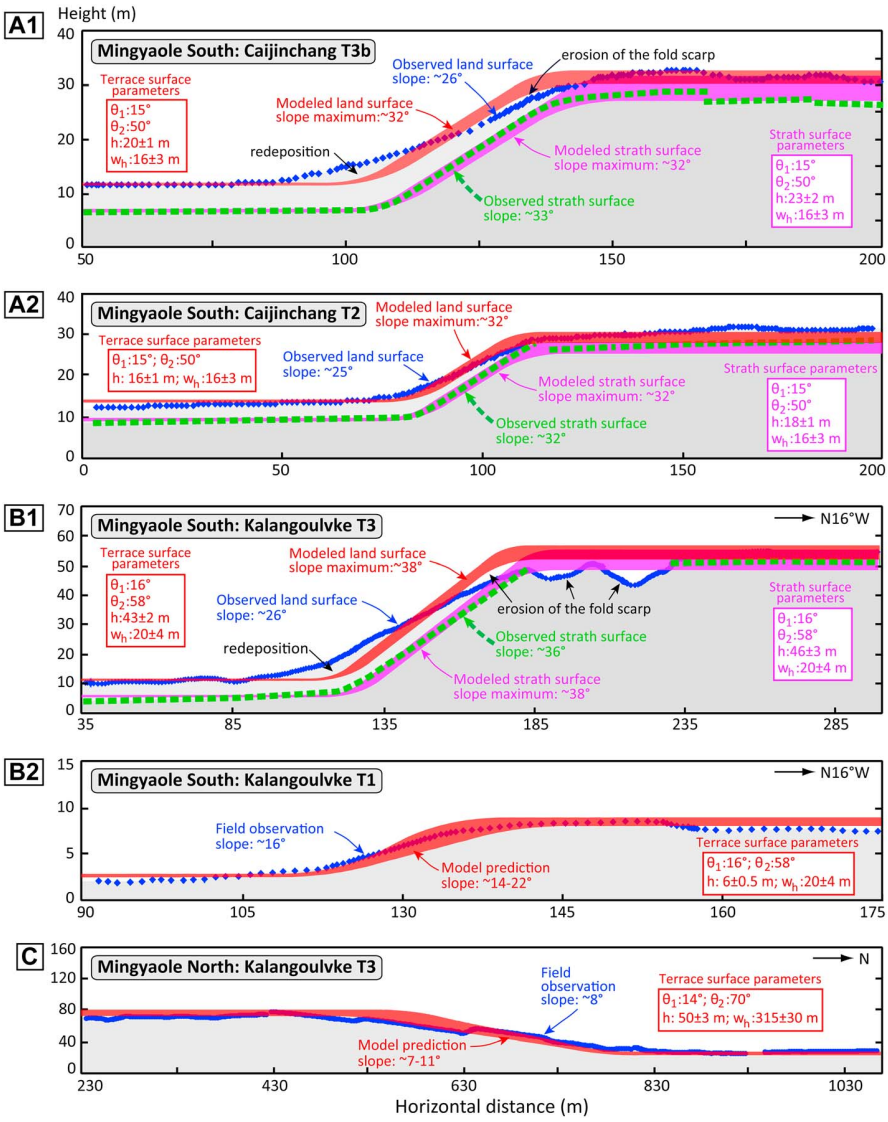

Figure 10. Field observation versus model prediction of the Mingyaole fold scarps. The modeled shape (red and pink lines, a change of thickness reflecting the modeling uncertainty) is predicted based on observed scarp height (H), hinge width (w_h), and underlying bed dips (θ_1 and θ_2). (A1, A2, and B1) For Caijinchang T3b and T2 and Kalangoulvke South T3, although the fold scarp on the land surface do not match well due to local erosion and deposition, the fold-scarp geometry represented by the strath surface quite closely mimics the model predictions. (B2 and C) For fold scarps on Kalangoulvke South T1 and Kalangoulvke North T3, field observations broadly match the model predictions.

observed fold scarps reveals a clear overall correlation in which mismatches result primarily either from erosion of the terrace surface or deposition across the fold hinge (Figure 10).

For the older terraces at Caijinchang (T3 and T2) and Kalangoulvke South (T3), the hinge migration distance is ~44 m, ~35 m, and 87 m, respectively, ~280%, ~220%, and ~440% of the hinge width of ~16–20 m (Table 2). Notably, the hinge has totally exited from its original position, and the ~32–36° slope on the strath surfaces closely approximates the modeled maximum slope of $32 \pm 6°$ (2σ) at Caijinchang and $38 \pm 6°$ (2σ) at Kalangoulvke South estimated from equation (7) (Figure 10a and Appendix B1). For the youngest terrace at Kalangoulvke South (T1), the hinge only migrates ~60% of hinge width from its original position, and the ~16° slope is smaller than the modeled maximum slope of $38 \pm 6°$(2σ), but can roughly match with the predicted slope of ~14–22° (Figure 10b2). At Kalangoulvke North, the hinge migrates ~85 m for the T3 fold scarp, similar to T3 fold scarp at Kalangoulvke South. However, the ratio of hinge migration/hinge

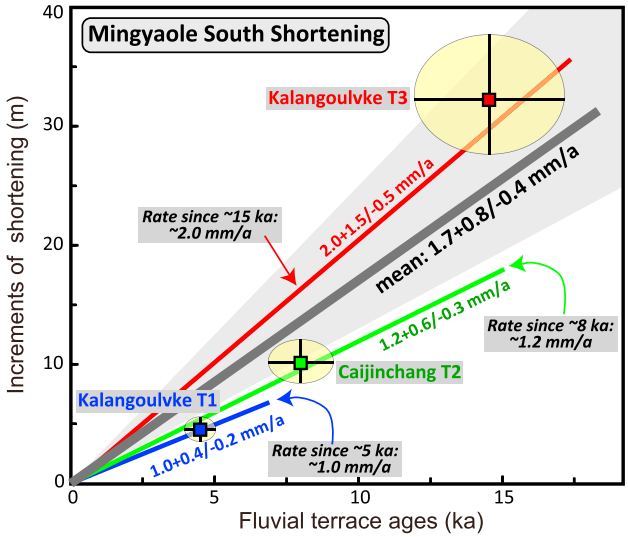

Figure 11. Shortening increment versus OSL ages of fluvial terraces on Mingyaole south limb, which yields a roughly constant (black solid line) or gradually decreasing (colored lines) shortening rate since abandonment of terrace T3 at ~15 ka. The shortening increments and rates are calculated from Monte Carlo simulations (Appendix B). Note that the age of Kalangoulvke T3 and T1 is the average age of OSL samples taken from each terrace (see text).

width is only ~30% due to the large hinge width of ~315 m (Figure 9). This limited migration produces a much smaller T1 slope of ~8° compared with both the ~36° T3 slope at Kalangoulvke South and its modeled maximum slope of 51 ± 7° (2σ) but is approximately consistent with the predicted slope of ~7–11° (Figure 10c).

Notably, in the analysis, the flexural-slip fault (FSF) scarps preserved on the upper tread of fold scarps are neglected in modeling. FSFs can affect both the fold-scarp height and slope [*Li et al.*, 2015]: impacts that would violate the basic assumptions of our model. Although the overall impact of the flexural-slip faults is difficult to estimate, the much smaller height (~0.2–4.2 m) of FSF scarps compared to the height (~6–55 m) of fold scarps (Figures 6, 7, and 9) and the minor discrepancies (Figure 10) between modeled and observed results suggest that these secondary faults have not significantly affected the first-order geometry of the fold scarp.

5.2. Incremental Shortening and Rate of the Mingyaole Fold

The incremental shortening absorbed by fold scarps can be quantified based on equation (6) (Table 2). Along the Kalangoulvke River valley that is located ~6–8 km to the east of the fold midpoint (Caijinchang site), the incremental shortening of the T3 fold scarp is $32.2^{+5.4/-4.5}$ m (2σ, Monte Carlo simulation result; see Appendix B) on the south limb and $44.6^{+9.1/-7.2}$ m (2σ) on the north limb, respectively, yielding a total shortening of ~77 m since abandonment of the T3 surface. Using the OSL age of 14.6 ± 2.6 ka, the shortening rate of fold scarps on the south and north limbs are $2.0^{+1.5/-0.5}$ mm/a (2σ) and $2.9^{+2.0/-0.7}$ mm/a (2σ), respectively, and the total shortening rate absorbed by these two fold scarps is ~5.0 mm/a. Because our model only can constrain the minimum incremental shortening, the shortening rate of the Mingyaole fold should be ≥5.0 mm/a. This rate is much larger than the average rate of ~1.1–1.9 mm/a since fold initiation at ~1.6 Ma, implying that the deformation rate has significantly increased during growth of the fold. At the longitude of the Mingyaole fold, the modern convergent rate is ~7–10 mm/a across the southern Tian Shan-Pamir interference zone [*Yang et al.*, 2008; *Zubovich et al.*, 2010; *Li et al.*, 2012]. Our study suggests that at least a half of regional shortening since ~15 ka has been absorbed by the Mingyaole fold. This rate is also quite close to the average shortening rate of ~5.0 mm/a of the Atushi-Kashi fold belt since ~1.2 Ma [*Scharer et al.*, 2004; *Heermance et al.*, 2008], indicating that, at the Mingyaole longitude, almost all of the shortening of the fold belt may be concentrated on this anticline, at least since ~15 ka.

In recent times, however, this rate appears to be decreasing (Figure 11). On the south limb, although Kalangoulvke and Caijinchang sites are ~6–8 km apart on the ~35 km long fold (Figure 5a), which could potentially lead to as much as ~20% difference (the total length divided by the apart distance) in their estimated rate of shortening, fold scarps at these two sites can provide a constraint of approximate changing tendency of the shortening rate. The incremental shortening of fold scarps on Caijinchang T2 and Kalangoulvke T1 terraces is $10.1^{+1.9/-1.6}$ m (2σ) and $4.5^{+1.0/-0.9}$ m (2σ), respectively. According to the ages of terrace surfaces, the shortening either maintains a roughly constant rate of $1.7^{+0.8/-0.4}$ mm/a (2σ) or decreases from $2.0^{+1.5/-0.5}$ mm/a since ~15 ka (Kalangoulvke T3) to $1.2^{+0.6/-0.3}$ mm/a since ~8.0 ka (Caijinchang T2) and $1.0^{+0.4/-0.2}$ mm/a since ~4.5 ka (Kalangoulvke T1). We prefer the latter interpretation

that the rate is gradually decreasing, and the shortening absorbed by the Mingyaole fold may be absorbed by other structures in the region.

6. Conclusion

Through an analysis of bed geometry migrating through the hinge, we develop a hinge-migrated fold-scarp model independent of specific fold-type and subsurface geometries. This model reveals kinematic processes of fold-scarp development that are similar to those of the classical fault-bend fold-scarp model [*Y. Chen et al.*, 2007; *Hubert-Ferrari et al.*, 2007; *Yue et al.*, 2011; *Le Béon et al.*, 2014]: the shape and slope are strongly controlled by changes in limb dips and hinge width (or the ratio of hinge migration distance/hinge width), but the scarp height is independent of the hinge width and can be used to calculate the incremental shortening absorbed by the fold scarp and its associated migrating hinge. Despite the presence of numerous flexural-slip faults associated with some of the fold scarps, robust estimates of bed migration through fold hinges is feasible. Application of this model to Mingyaole fold scarps in western China indicates that the modeled fold-scarp geometry can quite closely match field observations. Successful application of quantified outputs from this model, such as displacements or rates (when ages are known), depends on the presence of deformed geomorphic markers, such as river or marine terraces that have known initial geometries and whose preserved surfaces are deformed during fold growth. Whereas this model places limits only on the minimum fold shortening, rather than its total shortening, it provides a convenient method to discretely quantify the deformation of individual folds or fold bends and to analyze folding kinematics, even in the absence of strong constraints on overall subsurface structure of a fold.

Appendix A: Fold-Scarp Geometries With Curved-Hinge Migration

We derive geometric relationships for the height, incremental shortening, shape, and slope of the fold scarp with curved-hinge migration, and we demonstrate the equivalency of the "*maximum slope*" formula of our model to the classical fault-bend fold-scarp model [*Y. Chen et al.*, 2007; *Hubert-Ferrari et al.*, 2007].

We consider the curved hinge to be approximated by the arc of a circle with radius R (Figures A1 and A2). On either side of the hinge, the bed has dips of θ_2 (steeper) and θ_1 (gentler). From trigonometric relationships, we have

$$\gamma = (\pi - \theta_1 - \theta_2)/2$$
$$R = w_h \cdot \sin\gamma/2\cos(\gamma + \theta_1),$$

where γ is the angular difference between axial surface and undeformed land surface and w_h is the hinge width.

A1. Fold-Scarp Height and Incremental Shortening With Hinge Migration

First, we derive the formula of the slip-vector maximum (V). When the hinge migrates L (<hinge width, w_h) from position 1-1′ to 2-2′, the bed and terrace surface move along hinge-parallel slip vectors relative to their segments to the left of the hinge (Figure A1a). The points O' (circle center), A', and B' prior to hinge migration are, respectively, correlated with the points O, A, and B after hinge migration (Figure A1a inset). Then we have

$$\frac{AA'}{\sin\gamma} = \frac{L}{\sin(\pi - \gamma - \theta_1)}$$
$$\frac{BB'}{\sin(\pi - \gamma - \theta_2)} = \frac{V}{\sin(\theta_2 - \theta_1)}.$$

Given that $AA' = OO' = BB'$, we have the formula of the slip-vector maximum (V):

$$V = L(\sin\theta_2 - \sin\theta_1)/\cos\left(\frac{\theta_2 - \theta_1}{2}\right).$$

The fold-scarp height (H) and incremental shortening (S), which are, respectively, equal to the vertical and horizontal components of the slip-vector maximum, can be expressed by (Figure A1a)

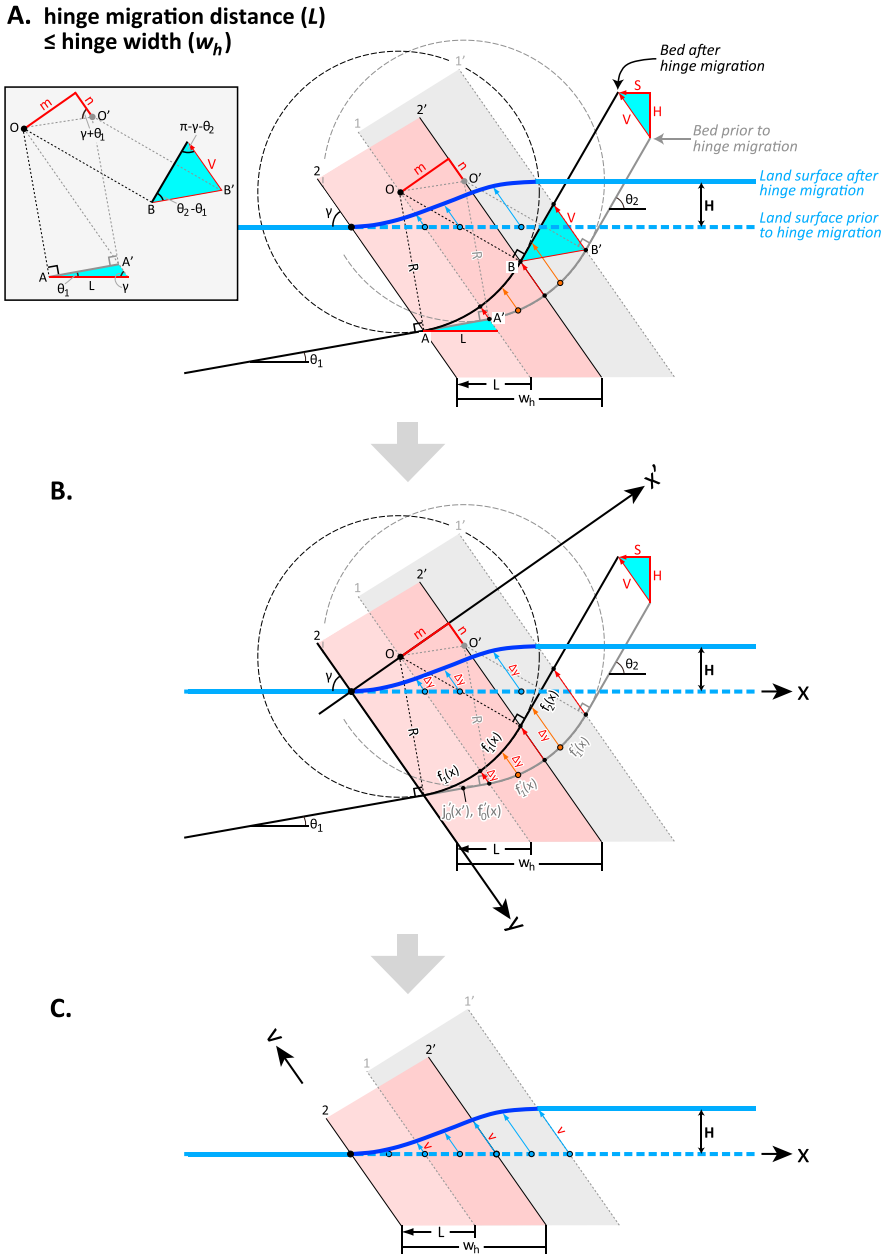

Figure A1. Active fold-scarp geometry with curved-hinge migration distance (L) smaller than the hinge width (w_h). (a) Geometric relationship of the bed and overlying terrace surface prior to and after hinge migration. Inset shows the correlation between $O'A'B'$ and OAB. This figure corresponds to Figure 3b2. (b) All materials set into an oblique frame reference with the y axis parallel to the hinge. (c) The relationship between the slip vector (v) with the horizontal distance (x).

$$H = V\sin\gamma = L\cdot\cos\left(\frac{\theta_2+\theta_1}{2}\right)(\sin\theta_2-\sin\theta_1)/\cos\left(\frac{\theta_2-\theta_1}{2}\right),$$

$$S = V\cos\gamma = L\cdot\cos\left(\frac{\theta_2+\theta_1}{2}\right)(\cos\theta_1-\cos\theta_2)/\cos\left(\frac{\theta_2-\theta_1}{2}\right).$$

Similarly, when the hinge migrates a distance larger than its width (Figure A2), the slip-vector maximum, fold-scarp height, and incremental shortening have the same formulas as above.

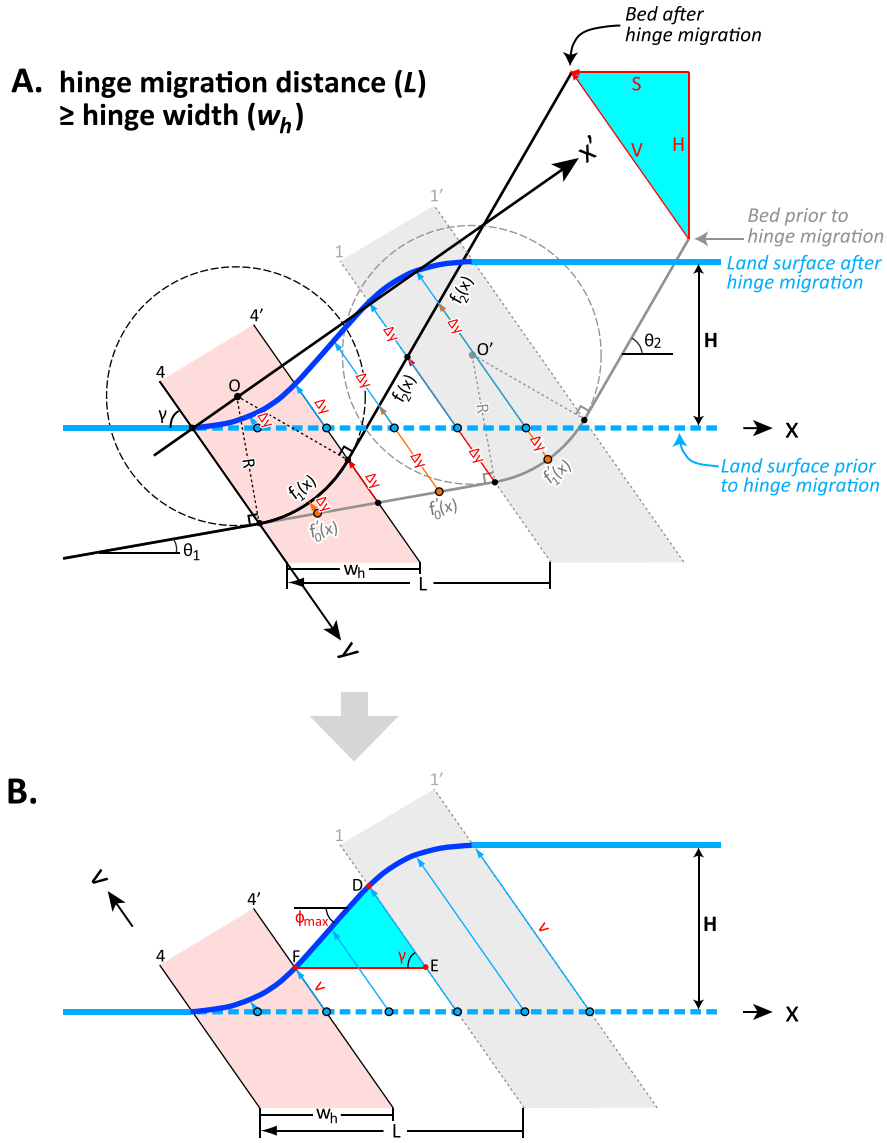

Figure A2. Active fold-scarp geometry with curved-hinge migration distance (L) larger than the hinge width (w_h). Note that the slope has reached its maximum (ϕ_{max}). This figure corresponds to Figure 3b4. See Figure A1 for descriptions.

A2. Formulas of the Shape and Slope

Then, we derive the shape and slope of the fold scarp. We put the bed and terrace surface into an oblique reference frame (x', y) as shown in Figures A1b and A2a, whose y axis is parallel to the hinge. The circle centers O' and O, respectively, have coordinates ($R\cos(\theta_1+\gamma)$, 0) and ($R\cos(\theta_1+\gamma)+m$, n), where m and n can be calculated from (Figure A1a inset)

$$m = OO'\sin(\gamma+\theta_1) = AA'\sin(\gamma+\theta_1) = L\sin\gamma$$
$$n = OO'\cos(\gamma+\theta_1) = AA'\cos(\gamma+\theta_1) = L\sin\gamma/\tan(\gamma+\theta_1).$$

To the left of the active hinge, the linear bed segment prior to hinge migration can be expressed as

$$y = j_0'(x') = x'\cot(\gamma+\theta_1) + R\sin(\gamma+\theta_1).$$

Because $x' = x\sin\gamma$ (Figure A1b), where x is the horizontal distance to the origin point, then we have

$$y = j_0'(x') = j_0'(x\sin\gamma) = x\sin\gamma\cot(\gamma+\theta_1) + R\sin(\gamma+\theta_1).$$

We use $f'_0(x)$ to represent this formula:

$$y = f'_0(x) = x\sin\gamma\cot(\gamma+\theta_1) + R\sin(\gamma+\theta_1).$$

In the hinge zone, the arc bed segment prior to ($f'_1(x)$) and after ($f_1(x)$) hinge migration can be expressed as

$$y = f'_1(x) = \sqrt{R^2 - [x\sin\gamma - R\cos(\gamma+\theta_1) - L\sin\gamma]^2} + L\sin\gamma/\tan(\gamma+\theta_1)$$
$$y = f_1(x) = \sqrt{R^2 - [x\sin\gamma - R\cos(\gamma+\theta_1)]^2}.$$

To the right of the hinge, the linear bed segment after hinge migration can be expressed as

$$y = f_2(x) = x\sin\gamma\cot(\gamma+\theta_2) + \frac{1-\cos(\gamma+\theta_1)\cos(\gamma+\theta_2)}{\sin(\gamma+\theta_2)}R.$$

If the migration distance (L) of the hinge is smaller than the hinge width (w_h) (Figure A1), we have the slip vector (v, parallel to the hinge) as a function of the horizontal distance (x) (Figure A1c):

$$v = \Delta y = f(x,\theta_2,\theta_1,w_h,H) = \begin{cases} 0 & x \le 0 \\ f'_0(x) - f_1(x) & 0 \le x \le L \\ f'_1(x) - f_1(x) & L \le x \le w_h \\ f'_1(x) - f_2(x) & w_h \le x \le (L+w_h) \\ H/\sin\gamma & x \ge (L+w_h) \end{cases}.$$

If we put $v = N_v \cdot w_h$, $x = N_x \cdot w_h$ into above formulas, we can obtain the formula of the slip vector with normalized hinge width (N_v):

$$N_v = v/w_h = f\left(N_x,\ \theta_2,\ \theta_1,\ \frac{L}{w_h}\right) = \begin{cases} 0 & N_x \le 0 \\ \left[f'_0(N_x\cdot w_h) - f_1(N_x\cdot w_h)\right]/w_h & 0 \le N_x \le L/w_h \\ \left[f'_1(N_x\cdot w_h) - f_1(N_x\cdot w_h)\right]/w_h & L/w_h \le N_x \le 1 \\ \left[f'_1(N_x\cdot w_h) - f_2(N_x\cdot w_h)\right]/w_h & 1 \le N_x \le 1 + L/w_h \\ H/(w_h\cdot\sin\gamma) & N_x \ge 1 + L/w_h \end{cases},$$

where N_x represents the percentage of hinge width. Similarly, if the migration distance (L) of the hinge is larger than the hinge width (w_h) (Figure A2), we have the relationships

$$v = \Delta y = f(x,\theta_2,\theta_1,w_h,H) = \begin{cases} 0 & x \le 0 \\ f'_0(x) - f_1(x) & 0 \le x \le w_h \\ f'_0(x) - f_2(x) & w_h \le x \le L \\ f'_1(x) - f_2(x) & L \le x \le (L+w_h) \\ H/\sin\gamma & x \ge (L+w_h) \end{cases}$$

and

$$N_v = v/w_h = f\left(N_x,\ \theta_2,\ \theta_1,\ \frac{L}{w_h}\right) = \begin{cases} 0 & N_x \le 0 \\ \left[f'_0(N_x\cdot w_h) - f_1(N_x\cdot w_h)\right]/w_h & 0 \le N_x \le 1 \\ \left[f'_0(N_x\cdot w_h) - f_2(N_x\cdot w_h)\right]/w_h & 1 \le N_x \le L/w_h \\ \left[f'_1(N_x\cdot w_h) - f_2(N_x\cdot w_h)\right]/w_h & L/w_h \le N_x \le 1 + L/w_h \\ H/(w_h\cdot\sin\gamma) & N_x \ge 1 + L/w_h \end{cases}.$$

The formula

$$v = f_0^{'}(x) - f_2(x) \qquad w_h \le x \le L$$

defines a linear segment, and we can obtain the maximum slope (ϕ_{max}) of the fold scarp (Figure A2b):

$$\begin{aligned} &\frac{DE}{\sin\phi_{max}} = \frac{EF}{\sin(\pi-\gamma-\phi_{max})} \\ \Rightarrow &\frac{v(L)-v(w_h)}{\sin\phi_{max}} = \frac{L-w_h}{\sin(\pi-\gamma-\phi_{max})} \\ \Rightarrow &\tan\left(\phi_{max}-\frac{\theta_1+\theta_2}{2}\right) = 2\tan\left(\frac{\theta_2-\theta_1}{2}\right) - \tan\left(\frac{\theta_2+\theta_1}{2}\right). \end{aligned} \tag{A1}$$

A3. Equivalence of the Maximum Slope Formula of Two Fold-Scarp Models

Finally, we show that the maximum slope ϕ_{max} formula of the classical fault-bend fold scarp in Figure 1a,

$$\tan(\theta_2-\phi_{max}) = \frac{\sin\theta_1\cos\left(\frac{\theta_2-\theta_1}{2}\right)}{\cos\left(\frac{\theta_2+\theta_1}{2}\right) - \sin\theta_1\sin\left(\frac{\theta_2-\theta_1}{2}\right)}, \tag{A2}$$

derived by *Y. Chen et al.* [2007] is equivalent to the formula (A1). If we substitute

$$\begin{aligned} A &= \phi_{max} - \frac{\theta_1+\theta_2}{2}, \\ B &= \frac{\theta_2+\theta_1}{2}, \\ C &= \frac{\theta_2-\theta_1}{2} \end{aligned}$$

into formula (A2), the formula can be transformed to

$$\begin{aligned} &\tan(C-A) = \frac{\sin(B-C)\cos C}{\cos(B)-\sin(B-C)\sin C} \\ \Rightarrow &\tan(C-A) = \frac{\sin(B-C)\cos C}{\cos(B-C+C)-\sin(B-C)\sin C} \\ \Rightarrow &\tan(C-A) = \frac{\sin(B-C)\cos C}{\cos(B-C)\cos C - 2\sin(B-C)\sin C} \\ \Rightarrow &\tan(C-A) = \frac{\tan(B-C)}{1-2\tan(B-C)\tan C} \\ \Rightarrow &\frac{1}{\tan(C-A)} = \frac{1-2\tan(B-C)\tan C}{\tan(B-C)} \\ \Rightarrow &\frac{1}{\tan(C-A)} = \frac{1}{\tan(B-C)} - 2\tan C \\ \Rightarrow &\frac{1}{\tan(C-A)} = \frac{1-\tan C\tan B+2\tan^2 C}{\tan B-\tan C} \\ \Rightarrow &\frac{1}{\tan(C-A)} = \frac{1+\tan^2 C-\tan C(\tan B-\tan C)}{\tan B-\tan C} \\ \Rightarrow &\frac{1}{\tan(C-A)} = \frac{1+\tan^2 C}{\tan B-\tan C} - \tan C \\ \Rightarrow &\frac{1}{\tan(C-A)} + \tan C = \frac{1+\tan^2 C}{\tan B-\tan C} \\ \Rightarrow &\frac{1+\tan^2 C}{\tan C-\tan A} = \frac{1+\tan^2 C}{\tan B-\tan C} \\ \Rightarrow &\tan C-\tan A = \tan B-\tan C \\ \Rightarrow &\tan A = 2\tan C-\tan B. \end{aligned}$$

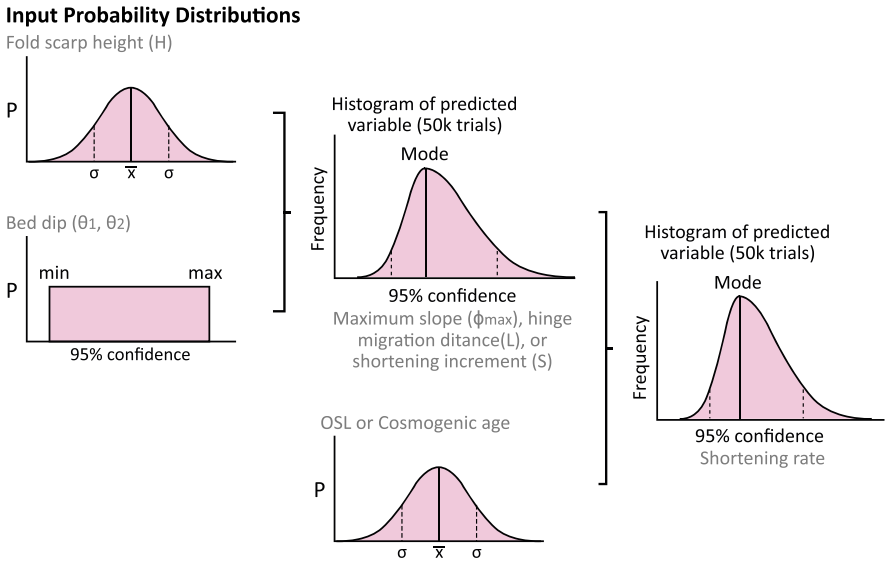

Figure B1. Schematic illustration of the Monte Carlo simulations used to estimate shortening increment and rate. This approach draws from a probability distribution of each input parameter to create a histogram of the predicted variable after 50,000 trials. Reported values represent the mode of the output histogram and the associated 95% confidence intervals. Input probability distributions include fold-scarp height (*H*), bed dips (θ_2 and θ_1), as well as OSL and cosmogenic ages. Appendix B contains further discussion of these parameters and predicted variable output.

Then the *A*, *B*, and *C* are substituted, and we have

$$\tan\left(\phi_{\max}-\frac{\theta_2+\theta_1}{2}\right)=2\tan\left(\frac{\theta_2-\theta_1}{2}\right)-\tan\left(\frac{\theta_2+\theta_1}{2}\right).$$

This formula is the same as formula (A1). Therefore, the formula (A1) is equivalent to the formula (A2).

Appendix B: Monte Carlo Simulation

The Monte Carlo simulations follow the approach of *Thompson et al.* [2002] and *Amos et al.* [2007] to estimate uncertainties of the shortening increment and rate (Figure B1). In our simulations, the probability distributions of each input parameter are sampled randomly from 50,000 trials to generate a frequency distribution. Reported values reflect the mode of the output histogram and the associated 95% confidence intervals.

Input parameters take into account fold-scarp height (*H*), bed dips (θ_2 and θ_1), as well as OSL and cosmogenic ages of terrace surfaces. For the fold-scarp height, we assign a normal distribution to characterize its mean and standard deviation. We assign a ±10% error to the bed dips. For the OSL and cosmogenic ages, a normal distribution is assigned to represent the mean and standard deviation. All simulations output lognormal distribution results.

Acknowledgments
Data used to support OSL dating of fluvial terraces at Kalangoulvke South (Figure 7) and topographic survey data of fold scarps (Figures 6, 7, and 9) are listed in Tables 1 and 2 and in the supporting information. This study was funded by China NSF (41302172), State Key Laboratory of Earthquake Dynamics of China (LED2010A04), the U.S. NSF (EAR 1050070), National S&T Major Project of China (2011ZX05003-002), and PetroChina Company (2014B0407). We thank W. Xiao and X. Yang for their help in the field work and J. Suppe, X. Wang, and D.F. He for supervising and fruitful discussions. Critical and thorough reviews of the manuscript by S. Dominguez and anonymous reviewers, the Associate Editor, and the Editor P. Tregoning significantly improved the current version.

References

Allmendinger, R. W. (1998), Inverse and forward numerical modeling of trishear fault-propagation folds, *Tectonics*, *17*(4), 640–656, doi:10.1029/98TC01907.

Amos, C. B., D. W. Burbank, D. C. Nobes, and S. Read (2007), Geomorphic constraints on listric thrust faulting: Implications for active deformation in the Mackenzie Basin, South Island, New Zealand, *J. Geophys. Res.*, *112*, B03S11, doi:10.1029/2006JB004291.

Chen, J., D. W. Burbank, K. M. Scharer, E. Sobel, J. Yin, C. Rubin, and R. Zhao (2002), Magnetochronology of the upper Cenozoic strata in the southern Chinese Tian Shan: Rates of Pleistocene folding and thrusting, *Earth Planet. Sci. Lett.*, *195*, 113–130.

Chen, J., K. M. Scharer, D. W. Burbank, R. Heermance, and C. S. Wang (2005a), Kinematic models of fluvial terraces over active fault-related folds: Constraints on the growth mechanism and kinematics [in Chinese], *Seismol. Geol.*, *27*, 513–529.

Chen, J., K. M. Scharer, D. W. Burbank, R. Heermance, and C. S. Wang (2005b), Quaternary detachment folding of the Mingyaole anticline, southwestern Tianshan [in Chinese], *Seismol. Geol.*, *27*, 530–547.

Chen, J., R. Heermance, D. W. Burbank, K. M. Scharer, J. Miao, and C. S. Wang (2007), Quantification of growth and lateral propagation of the Kashi anticline, southwest Chinese Tianshan, *J. Geophys. Res.*, *112*, B03S16, doi:10.1029/2006JB004345.

Chen, Y., K.-Y. Lai, Y.-H. Lee, J. Suppe, W.-S. Chen, Y.-N. N. Lin, Y. Wang, J.-H. Hung, and Y.-T. Kuo (2007), Coseismic fold scarps and their kinematic behavior in the 1999 Chi-Chi earthquake Taiwan, *J. Geophys. Res.*, *112*, B03S02, doi:10.1029/2006JB004388.
Epard, J. L., and R. H. Groshong (1993), Excess area and depth to detachment, *AAPG Bull.*, *77*(8), 1291–1302.
Erslev, E. A. (1991), Trishear fault-propagation folding, *Geology*, *19*, 617–620.
Feng, X. Y. (1994), Surface rupture associated with the 1985 Wuqia earthquake in Xinjiang, in *Research on Active Fault (3)* [in Chinese], pp. 45–55, Seismol. Press, Beijing.
Galbraith, R. F., and G. M. Laslett (1993), Statistical models for mixed fission track ages, *Nucl. Tracks Radiat. Meas.*, *21*, 459–470.
Goode, J. K., and D. W. Burbank (2011), Kinematic implications of consequent channels on growing folds, *J. Geophys. Res.*, *116*, B04407, doi:10.1029/2010JB007617.
Heermance, R. V., J. Chen, D. W. Burbank, and J. J. Miao (2008), Temporal constraints and pulsed late Cenozoic deformation during the structural disruption of the active Kashi foreland, northwest China, *Tectonics*, *27*, TC6012, doi:10.1029/2007TC002226.
Hubert-Ferrari, A., J. Suppe, R. Gonzalez-Mieres, and X. Wang (2007), Mechanisms of active folding of the landscape (southern Tian Shan, China), *J. Geophys. Res.*, *112*, B03S09, doi:10.1029/2006JB004362.
Ishiyama, T., K. Mueller, M. Togo, A. Okada, and K. Takemura (2004), Geomorphology, kinematic history, and earthquake behavior of the active Kuwana wedge thrust anticline, central Japan, *J. Geophys. Res.*, *109*, B12408, doi:10.1029/2003JB002547.
Ishiyama, T., K. Mueller, H. Sato, and M. Togo (2007), Coseismic fault-related fold model, growth structure, and the historic multisegment blind thrust earthquake on the basement-involved Yoro thrust, central Japan, *J. Geophys. Res.*, *112*, B03S07, doi:10.1029/2006JB004377.
Le Béon, M., J. Suppe, M. K. Jaiswal, Y. G. Chen, and M. E. Ustaszewski (2014), Deciphering cumulative fault slip vectors from fold scarps: Relationships between long-term and coseismic deformations in central Western Taiwan, *J. Geophys. Res. Solid Earth*, *119*, 5943–5978, doi:10.1002/2013JB010794.
Li, T., J. Chen, J. A. Thompson, D. W. Burbank, and W. P. Xiao (2012), Equivalency of geologic and geodetic rates in contractional orogens: New insights from the Pamir Frontal Thrust, *Geophys. Res. Lett.*, *39*, L15305, doi:10.1029/2012GL051782.
Li, T., J. Chen, J. A. Thompson, D. W. Burbank, and X. Yang (2013a), Quantification of three-dimensional folding using fluvial terraces: A case study from the Mushi anticline, northern margin of the Chinese Pamir, *J. Geophys. Res. Solid Earth*, *118*, 4628–4647, doi:10.1002/jgrb.50316.
Li, T., J. Chen, and W. P. Xiao (2013b), Late-Quaternary folding of the Mingyaole anticline southwestern tip, Pamir-Tianshan convergent zone [in Chinese], *Seismol. Geol.*, *35*, 234–246, doi:10.3969/j.issn.0253-4967.2013.02.004.
Li, T., J. Chen, J. A. Thompson, D. W. Burbank, and X. Yang (2015), Active flexural-slip faulting: A study from the Pamir-Tian Shan convergent zone, NW China, *J. Geophys. Res. Solid Earth*, *120*, 4359–4378, doi:10.1002/2014JB011632.
Molnar, P., and P. Tapponnier (1975), Cenozoic tectonics of Asia: Effects of a continental collision, *Science*, *189*, 419–426, doi:10.1126/science.189.4201.419.
Murray, A. S., and A. G. Wintle (2003), The single aliquot regenerative dose protocol: Potential for improvements in reliability, *Radiat. Meas.*, *37*, 377–381.
Novoa, E., J. Suppe, and J. H. Shaw (2000), Inclined-shear restoration of growth folds, *AAPG Bull.*, *84*(6), 787–804.
Poblet, J. (2012), 2D kinematic models of growth fault-related folds in contractional settings, in *Tectonics of Sedimentary Basin: Recent Advances*, edited by C. Busby and A. Azor, 1st ed., pp. 538–566, Wiley-Blackwell, West Sussex, U. K.
Poblet, J., and K. McClay (1996), Geometry and kinematics of single layer detachment folds, *AAPG Bull.*, *80*, 1085–1109.
Poblet, J., K. McClay, F. Storti, and J. A. Muñoz (1997), Geometries of syntectonic sediments associated with single-layer detachment folds, *J. Struct. Geol.*, *19*, 369–381.
Scharer, K. M., D. W. Burbank, J. Chen, R. J. Weldon, C. Rubin, R. Zhao, and J. Shen (2004), Detachment folding in the southwestern Tian Shan-Tarim foreland, China: Shortening estimates and rates, *J. Struct. Geol.*, *26*, 2119–2137.
Scharer, K. M., D. Burbank, J. Chen, and R. J. Weldon II (2006), Kinematic models of fluvial terraces over active detachment folds: Constraints on the growth mechanism of the Kashi-Atushi fold system, Chinese Tian Shan, *Geol. Soc. Am. Bull.*, *118*, 1006–1021, doi:10.1130/B25835.1.
Shaw, J. H., C. Connors, and J. Suppe (2005), *Seismic Interpretation of Contractional Fault-Related Folds*, *AAPG Stud. Geol.*, vol. 53, Am. Assoc. Pet. Geol., Tulsa, Okla.
Sobel, E. R., and T. A. Dumitru (1997), Thrusting and exhumation around the margins of the western Tarim basin during the India-Asia collision, *J. Geophys. Res.*, *102*(B3), 5043–5063, doi:10.1029/96JB03267.
Sobel, E. R., J. Chen, and R. V. Heermance (2006), Late Oligocene-Early Miocene initiation of shortening in the southwestern Chinese Tian Shan: Implications for Neogene shortening rate variations, *Earth Planet. Sci. Lett.*, *247*, 70–81, doi:10.1016/j.epsl.2006.03.048.
Suppe, J. (1983), Geometry and kinematics of fault-bend folding, *Am. J. Sci.*, *283*, 684–721.
Suppe, J., and D. A. Medwedeff (1990), Geometry and kinematics of fault-propagation folding, *Eclogae Geol. Helv.*, *83*, 409–454.
Suppe, J., G. T. Chou, and S. C. Hook (1992), Rates of folding and faulting determined from growth strata, in *Thrust Tectonics*, edited by K. R. McClay, pp. 105–121, CRC Press, Boca Raton, Fla.
Suppe, J., F. Sabat, J. A. Munoz, J. Poblet, E. Roca, and J. Verges (1997), Bed-by-bed fold growth by kink-band migration: Sant Llorenc de Morunys, eastern Pyrenees, *J. Struct. Geol.*, *19*(3–4), 443–461, doi:10.1016/S0191-8141(96)00103-4.
Thompson, J. A. (2013), Neogene tectonic evolution of the NE Pamir margin, NW China, PhD thesis, Univ. of Calif., Santa Barbara.
Thompson, J. A., D. W. Burbank, T. Li, J. Chen, and B. Bookhagen (2015), Late Miocene northward propagation of the northeast Pamir thrust system, northwest China, *Tectonics*, *34*, 510–534, doi:10.1002/2014TC003690.
Thompson, S. C., R. J. Weldon, C. M. Rubin, K. Abdrakhmatov, P. Molnar, and G. W. Berger (2002), Late Quaternary slip rates across the central Tien Shan, Kyrgyzstan, central Asia, *J. Geophys. Res.*, *107*(B9), 2203, doi:10.1029/2001JB000596.
Yang, S. M., J. Li, and Q. Wang (2008), The deformation pattern and fault rate in the Tianshan Mountains inferred from GPS observations, *Sci. China, Ser. D*, *51*(8), 1064–1080, doi:10.1007/s11430-008-0090-8.
Yeats, R. S., M. N. Clark, E. A. Keller, and T. K. Rockwell (1981), Active fault hazard in south California: Ground rupture versus seismic shaking, *Geol. Soc. Am. Bull.*, *92*, 189–196.
Yeats, R. S., K. S. Sieh, and C. R. Allen (1997), *Geology of Earthquake*, pp. 344–346, Oxford Univ. Press, New York.
Yin, A., S. Nie, P. Craig, T. M. Harrison, F. J. Ryerson, X. Qian, and G. Yang (1998), Late Cenozoic tectonic evolution of the southern Chinese Tian Shan, *Tectonics*, *17*(1), 1–27, doi:10.1029/97TC03140.
Yue, L.-F., J. Suppe, and J.-H. Hung (2011), Two contrasting kinematic styles of active folding above thrust ramps, Western Taiwan, in *Thrust Fault-Related Folding*, *AAPG Mem.*, vol. 94, edited by K. McClay, J. Shaw, and J. Suppe, pp. 153–186, AAPG, Tulsa, Okla., doi:10.1306/13251337m943431.
Zubovich, A. V., et al. (2010), GPS velocity field of the Tien Shan and surrounding regions, *Tectonics*, *29*, TC6014, doi:10.1029/2010TC002772.